Three-dimensional numerical simulation of a lab-scale pressurized fluidized bed using a soft-sphere DEM-CFD approach

Ainur Nigmetova, Enrica Masi, Olivier Simonin, Yann Dufresne, Vincent Moureau

Three-dimensional numerical simulation of a lab-scale pressurized fluidized bed using a soft-sphere DEM-CFD approach

Ainur Nigmetova[a], Enrica Masi[a,*], Olivier Simonin[a], Yann Dufresne[b], Vincent Moureau[b]

[a]*Institut de Mécanique des Fluides de Toulouse (IMFT), Université de Toulouse, CNRS, France*
[b]*CORIA UMR 6614 CNRS-INSA, Université de Rouen, 76801 Saint-Etienne du Rouvray, France*

Abstract

The present work is dedicated to the numerical study of the hydrodynamics of a pressurized fluidized-bed using an Euler-Lagrange approach. The gas phase is modeled by filtered Navier-Stokes equations, and the solid particles are tracked using a Discrete Element Method (DEM). Collisions are handled using a soft-sphere model. Numerical predictions of the mean (time-averaged) vertical particle velocity are compared with experimental measurements available from the literature, obtained from a Positron Emission Particle Tracking (PEPT) technique. In addition, Discrete Element Method (DEM)-Computational Fluid Dynamics (CFD) results are extensively compared with predictions from Two-Fluid Model (TFM) numerical simulations. Results accounting for inelastic frictionless particle-particle collisions show a very good agreement with the experimental data and Two-Fluid Model (TFM) results in the central zone of the reactor. In the near wall region the numerical simulation overestimates the downward particle velocity with respect to the experimental measurements, especially when the particle-wall friction is neglected. The influence of the friction at the wall is therefore further investigated and a local analysis of the particle-wall interactions is carried out. It is demonstrated that the long sustained contacts of particle clusters with the wall in such a dense regime play a crucial role on the overall bed behavior. Therefore, this effect should be taken into account in the boundary conditions of a TFM approach when it is used to predict bubbling fluidized beds.

Keywords:
Gas-solid flows, dense fluidized bed, boundary conditions, DEM-CFD

1. Introduction

The aim of this work is to reproduce the physical behavior of a dense pressurized gas-solid fluidized bed at mesoscopic scale in order to extract information to use in macroscopic modeling. Fluidized beds are indeed central to many applications in industry, and they are quite challenging to model because of the large dimensions of the industrial devices compared to the characteristic length scales of the particulate flow. Additional constraints are often introduced for modeling approaches due to the wide range of time scales related to the physical phenomena occurring in such processes. Such scales depend on several factors, as the properties of the particle and fluid phases (mean particle size, densities, viscosity, etc.), the mechanisms involved (melting, evaporation, homogeneous/heterogenous combustion, etc.), the operating points (velocities, temperatures, pressures, etc.) which also affect the macroscopic flow properties. Accurate prediction of the fluidized bed hydrodynamics at industrial scale is still an

*Corresponding author
Email address: enrica.masi@imft.fr (Enrica Masi)

open question which requires further detailed experiments in order to assess the macro-scale numerical strategies. With macroscopic modeling we mean unsteady three-dimensional (3D) CFD to use at industrial scale, which differs from 1D/1.5D approaches that are reduced-order macroscopic models, and from 0D approaches that are process (or network) models. The most commun modeling used for macro-scale numerical predictions is the Euler-Euler approach (also referred to as N-Euler approach, when more than two phases are involved), most usually known as TFM. In collisional/dense regimes, closures are provided in the frame of the Kinetic Theory of Granular Flows (KTGF) (Jenkins and Savage (1983)). A very extensive literature exists on this subject. For details about its fundamentals (averaged methods, constitutive relations, etc.), and applications to the fluidization, the reader is referred to the work of Gidaspow (1994).

Models used in CFD at macroscopic scale rely on the modeling of the local effects which take place at microscopic scale (smaller than the particle size). Micro-scale (particle-resolved) numerical simulations are however constrained to very small size systems and may be used to address fundamental questions in very simple geometry and limited number of particles (Tenneti and Subramaniam (2014); Deen et al. (2014)). Improved accuracy with respect to macro-scale models may be obtained at mesoscopic scale, where the fluid is not fully resolved around each particle, as in microscopic simulations, but rather modeled in a local-average way larger than the mean particle size. Momentum, for exemple, is not exchanged between the particle and the fluid through the boundary layer surrounding each particle, but rather modeled by an inter-phase drag term accounting for the whole effect of the particles contained in a selected volume (properly weighted). The fluid-to-particle coupling is in turn affected by the local approximation of the fluid flow at the particle location. Nevertheless, no further assumptions are introduced for the particulate phase with respect to a microscopic approach and, for sufficiently refined grids (or accounting for reliable sub-grid scale models), results provide a trusted representation of the local and instantaneous behavior. In collisional regime, where particle-particle interactions play the major role, a DEM (also referred to distinct element or discret particle method) should be used in conjunction with CFD. This method stands as an alternative to the simpler Discrete Particle Simulation (DPS), which is a point-particle approach only appropriate for very small particle in dilute regime, and usually employed in dilute particle-laden turbulent flows (Balachandar and Eaton (2010); Kuerten (2016)). DEM-CFD is an Euler-Lagrange approach, where filtered Navier-Stokes equations (in a spatial average sense) are solved for the gas phase, and particles are tracked individually taking collisions and external forces acting on the particles directly into account. The filtered kernel should be larger than the particle size and smaller than the characteristic length scales of the flow, in order to comply with the scale separation (Pepiot and Desjardins (2012)).

DEM was first developed by Cundall and Strack (1979). Later on, coupling methods with the Navier-Stokes equations (CFD) were proposed using both soft-sphere (Tsuji et al. (1992, 1993)) and hard-spere (Hoomans et al. (1996)) collision models. These models are two different way to compute collisions in particulate flows (Schwarzkopf et al. (2011)). Both have advantages and drawbacks. The hard-sphere model is better suited to dilute regimes since collisions are assumed to be binary and instantaneous and therefore require to be treated one after the other. The soft-sphere model is instead preferable in dense regimes since it makes it possible to simulate multiple contacts and to take into account additional particle-particle interaction forces (as cohesive ones), which are easier to implement than in a hard-sphere model (van der Hoef et al. (2006)). With regard to the computational efficiency, the hard-sphere model is significantly faster than the soft-sphere model for dilute systems, while the soft-sphere model remains numerically efficient in dense gas-particle flow in which the particle running time between two successive collisions is close to the contact duration of a collision (van der Hoef et al.

(2006)).

Since the seminal work of Cundall and Strack (1979), the DEM approach has been extensively used to study particulate flows in dense regimes, also thanks to its implementation in open-sources codes (Li et al. (2012); Kloss et al. (2012)). Most of the works find their applications in chemical engineering, especially the studies of bubbling fluidized beds (Xu and Yu (1997); Kawaguchi et al. (1998); Hamidouche et al. (2019)), accounting for additional physics as inter-particle cohesive interactions (Mikami et al. (1998)), heat exchanges (Patil et al. (2015), Li et al. (2017)) or reactions (Kaneko et al. (1999), Sutkar et al. (2016)). DEM-CFD has also largely been employed in industry (on reduced configurations) to deepen some fundamentals of the production processes (see, for exemple, the studies of granular beds with lateral injections for applications to the steel industry (Feng et al. (2003)).

Several works have employed DEM-CFD to analyze the effects of some parameters, especially those not accessible from experiments (at least in a distinct way). For exemple, a characterization of the flow structure was carried out by Li and Kuipers (2007), who studied the effects of the particle-particle versus the fluid-particle interactions by varying both collision parameters (friction and restitution coefficients) and fluid velocity, on a 2D fluidized bed configuration. The effect of the rolling friction, to reproduce the particle non-sphericity, was investigated by Goniva et al. (2012) in a quasi-2D spout-fluidized bed using DEM-CFD. A large number of combined numerical and experimental studies have also been carried out. For exemple, Yuu et al. (2000) performed numerical simulations of a quasi-2D bubbling fluidized bed using DEM-CFD, and provided comparisons with their experiments through the mean pressure drop and the mean and fluctuating vertical particle velocity. The latter was obtained by an original technique detecting colored particles and recording their trajectories. Link et al. (2005) used DEM-CFD to reproduce an experimental (quasi-2D and 3D) spout-fluidized bed and characterize the different regimes appearing in such a configuration. Drag models were assessed against experimental results and a mesh analysis carried out to evaluate a new inter-phase coupling technique. Müller et al. (2008) used Magnetic Resonance (MR) to extract the mean vertical particle velocity and the granular temperature from an experimental fluidized bed. Numerical simulations were then performed using a DEM-CFD approach and results compared to the experimental measurements; the effect of the restitution coefficient and the bed thickness was further analyzed. van Buijtenen et al. (2011) carried out experiments on a quasi-2D triple-spout fluidized bed by using both Particle Image Velocimetry (PIV) and Positron Emission Particle Tracking (PEPT) techniques and compared the time-averaged particle velocity with the predictions of DEM-CFD numerical simulations. Neuwirth et al. (2013) used DEM-CFD to simulate a rotor granulator, then comparing with experimental averaged particle velocity obtained by a new non-intrusive experimental technique (Magnetic Particle Tracking (MPT)) allowing to track the position of a magnetized particle. The aforementioned works represent only some of the numerous studies carried out on the hydrodynamic characterization of the particulate flow in fluidized beds, using a DEM-CFD approach. A broader overview may be found in the works of Deen et al. (2007), Zhu et al. (2007), Zhu et al. (2008), and Guo and Curtis (2015).

An extensive literature also exists about the use of the DEM-CFD approach to assess theory and modeling developed in the frame of a TFM approach. For exemple, Goldschmidt et al. (2002) used the DEM-CFD to extract particle velocity and impact velocity distributions, comparing with those modeled in the frame of the kinetic theory of granular flows, analyzing deviations due to inelastic collisions. Schneiderbauer et al. (2012) proposed a new closure for the particle stress tensor accounting for frictional effects, effective in both frictional and collisional regimes. Assessments were done by comparing Eulerian simulations with an in house

experiment (a discharge of a rectangular bin) and with DEM-CFD and experiments of a quasi-2D triple-spout fluidized bed (van Buijtenen et al. (2011)). Yang et al. (2017) studied the effect of both restitution and friction coefficients using TFM, accounting explicitly for both rotation and friction in the particulate phase. The model was assessed comparing with DEM-CFD numerical results.

The DEM-CFD approach has been so successful that its formulation has been improved over the years, especially with regard to numerical efficiency and computing performances. For example, Jajcevic et al. (2013) proposed a numerical strategy based on the coupling of CFD and DEM by running, respectively, on CPU and GPU systems (simulating up to 25 million particles). OpenMP (Amritkar et al. (2014)) or hybrid MPI/OpenMP (Berger et al. (2015)) parallelizations were also proposed as an alternative. Buist et al. (2016) developed a hybrid soft/hard sphere model to improve both efficiency and accuracy of DEM-CFD. The model was successfully tested up to one million particles and 50% of solid volume fraction. Several sophisticate techniques have been further developed in the last years, so that nowadays it is possible to carry out numerical simulations with tens of millions or even a few hundred million particles (Pepiot and Desjardins (2012), Capecelatro and Desjardins (2013), Dufresne et al. (2019)) on more realistic reactors, up to the pilot scale. This is of extreme importance because, due to the limited information available from experiments, DEM-CFD offers a unique strategy allowing to gain knowledge in the local and instantaneous behavior of dense particulate flows.

In the present study, we use the DEM-CFD numerical simulations in order extract information to use in macroscopic models. This way to proceed is part of a multi-scale numerical strategy, which relies on the information obtained at smaller scales (here mesoscopic) to characterize and model the flow at larger scales. Indeed, the strength of a DEM-CFD approach is to allow the CFD to provide accurate solutions in unsteady-flows configurations and complex geometries of dimensions much larger than the particle size, so allowing to capture physical mechanisms related to the collective motion and large scale interactions. However, when the scale separation becomes too large, typically at industrial scale, such an approach cannot be employed because of its excessive computational cost. A macroscopic modeling is therefore mandatory. Numerical simulations of industrial-scale fluidized beds are mostly performed using a TFM approach, which requires many hypotheses, in particular on the modeling of the particle-particle and particle-wall collisions. To validate these macro-scale assumptions and to increase the predictive capabilities of this modeling, an investigation at mesoscopic scale is carried out. In particular, we focus on the characterization of the effects of the solid-solid contact on the overall bed behavior. Because of the numerous parameters involved in a solid-solid collision (material of the particles and walls, particle shape, wall roughness, etc.), it is not obvious to establish a generally applicable modeling for the macroscale numerical simulations only on the basis of the experimental results. Unlike experimental investigations, DEM-CFD makes it possible to separate each effect in order to help to improve understanding and thus to develop more suitable macroscale models.

According to Johnson and Jackson (1987), particulate flows may exhibit either short or long contact duration depending on the particulate regime and flow conditions. A short contact relies on elastic or inelastic collisions, in the presence or not of dynamic frictional effects. A long contact instead implies long-lasting normal reaction forces occurring between sliding solids, which produce tangential forces in the presence of solid-solid friction. The latter refers to a frictional shear stress effect, often discarded in the TFM modeling of fluidized beds. Such an effect may instead have a substantial influence especially at low fluidization velocities (Patil et al. (2005a,b)). A very extensive literature exists on the development of boundary conditions for particulate (granular rapid) flows, especially focus on modeling the collisional contribution

in the presence of smooth or rough walls, with or without dynamic friction (see, e.g. Hui et al. (1984); Jenkins (1992); Sommerfeld and Huber (1999); Sakiz and Simonin (1999); Konan et al. (2009); Soleimani et al. (2015); Radenkovic and Simonin (2018)). Instead, particle-wall frictional shear stress effects are generally neglected in collisional regimes, as in most of fluidized bed configurations, because the mean solid volume fraction is globally lower than a threshold value. This value ($\alpha_{p,min} \geq 0.5$) was introduced by Johnson et al. (1990) on the basis of empirical observations. Adding the two short and long contact effects, Johnson and Jackson (1987) and Johnson et al. (1990) proposed a model to reproduce the whole contribution to the total stresses in intermediate regimes, close to the wall as well as in internal regions of the flow. In particular, they proposed a boundary condition accounting for both short and long contact effects, neglecting the dynamic friction during collisions while accounting for the rough wall effect by introducing a specularity coefficient. In the present study, the effect of the particle-wall friction, as well as of the particle-particle normal restitution coefficient, on the overall hydrodynamic behavior of the pressurized fluidized-bed pilot is analyzed. Numerical results are compared with experimental measurements available from the literature (Fede et al. (2009)) and with macroscale numerical predictions (Fede et al. (2016)), in order to evaluate existing TFM assumptions (Balzer et al. (1995), Boelle et al. (1995)), including boundary conditions. From a local analysis of the particle-wall interactions, it is shown that the long contact effects cannot be neglected in boundary conditions of bubbling fluidized beds because of the presence of high concentration of particles near the wall, which may be very effective in the presence of smooth walls as well. Accordingly, the boundary condition model for the particle velocity wall-tangential component is written accounting for the long sustained contacts of the particle clusters in dense regime (as introduced by Johnson and Jackson (1987)), for smooth walls. It additionally includes, unlike Johnson and Jackson's boundary condition, the effects of the dynamic friction in the presence of sliding collisions on flat walls (Sakiz and Simonin (1999)). The frictional contribution to the particle-wall shear stress then can be closed using the original model proposed by Johnson et al. (1990), with same or different empirical parameters (Ocone et al. (1993)), or more sophisticated closure (see, e.g. Schneiderbauer et al. (2012) and references cited in). The boundary condition model and the particle-wall interactions investigated in the present study are presented and discussed in Section 5. In Section 2 the DEM-CFD approach used in this work is briefly recalled, together with the technique employed to obtain Eulerian particle mesoscopic fields from Lagrangian data. Numerical simulations are detailed in Section 3 and their results discussed in Section 4. Conclusions are given at the end in Section 6.

2. Numerical strategy

The DEM-CFD numerical strategy adopted in the present study is here briefly recalled (Dufresne et al. (2020)). This methodology has been implemented in the finite-volume code YALES2 based on a double domain decomposition allowing to handle complex geometry on massively parallel machines (Moureau et al. (2011)). YALES2 solves the low-Mach Navier-Stokes equations on unstructured meshes, by a fourth-order scheme both in space and time. A second-order scheme is also available and it was retained in our study. Particle-laden flows are enabled by coupling with the DEM approach, through the YALES2 granular solver (Dufresne et al. (2016, 2019, 2020)). The way to obtain mesoscopic particle field and macroscopic particle quantities from Lagrangian DEM-CFD numerical results is also detailed at the end in Section 2.2.

2.1. DEM-CFD for numerical simulations at mesoscopic scale

2.1.1. Gas phase modeling

The governing equations for the gas phase are obtained by spatially filtering the unsteady, low-Mach number, Navier-Stokes equations (NS) equations (Capecelatro and Desjardins (2013)). A filtering operation is formally introduced to account for the smallest scale interactions. Particles are indeed smallest than the resolved fluid length scale, which in fact implies filtered NS equations. The framework is similar to that of the Large-Eddy Simulation (LES). This is why the approach if often referred to as DEM-LES (Dufresne et al. (2016)) and may be used accounting for additional sub-grid scale models if needed. Introducing G as the filtering kernel with a characteristic length Δ_f, the local instantaneous fluid volume fraction is defined as $\alpha_g(\mathbf{x},t) = \int_{V_f} G(\mid \mathbf{x}-\mathbf{y} \mid)d\mathbf{y}$, where V_f is the volume occupied by the fluid. Defining $c_g(\mathbf{x},t)$ as any local and instantaneous unfiltered fluid property, the volume filtered field $\widehat{c}_g(\mathbf{x},t)$ refers to the spatial average which is computed by taking the convolution product with the filtering kernel G, leading to write $\alpha_g\widehat{c}_g(\mathbf{x},t) = \int_{V_f} c_g(\mathbf{y},t)G(\mid \mathbf{x}-\mathbf{y} \mid)d\mathbf{y}$. The density-weighted Favre average is then defined as $\breve{c}_g(\mathbf{x},t) = \alpha_g\widehat{\rho_g(\mathbf{x},t)c_g(\mathbf{x},t)}\,/\alpha_g\widehat{\rho_g(\mathbf{x},t)}$. In absence of heat and mass transfers, the governing equations for the fluid read

$$\frac{\partial}{\partial t}(\alpha_g\widehat{\rho}_g) + \nabla\cdot(\alpha_g\widehat{\rho}_g\breve{\mathbf{u}}_g) = 0 \tag{1}$$

$$\frac{\partial}{\partial t}(\alpha_g\widehat{\rho}_g\breve{\mathbf{u}}_g) + \nabla\cdot(\alpha_g\widehat{\rho}_g\breve{\mathbf{u}}_g\otimes\breve{\mathbf{u}}_g) = -\nabla\widehat{P}_g + \nabla\cdot(\alpha_g\widehat{\tau}_g) + \alpha_g\widehat{\rho}_g\mathbf{g} + \mathbf{I}_{p\to g}, \tag{2}$$

where $\breve{\mathbf{u}}_g$, $\widehat{\rho}_g$, $\widehat{P}_g$ are respectively the fluid velocity, density and pressure, $\mathbf{g}$ is gravity and $\widehat{\tau}_g$ is the stress tensor accounting for both viscous and sub-grid contributions (when taken into account). Hereafter, to simplify the writing, the filtering notation will be dropped out and $\mathbf{u}_g$, ρ_g and P_g will refer to filtered fields. $\mathbf{I}_{p\to g}$ represents the momentum transfer from the particles to the fluid. Its modeling will be detailed later in Section 2.1.3. These equations are supplemented by the ideal gas equation of state.

2.1.2. Solid phase modeling

In this work, the solid phase is composed of mono-disperse spherical particles. In the DEM modeling, particle position and velocity are known for each individual particle and tracked in a Lagrangian way. The translation motion of a spherical particle p of mass m_p is given by Newton's second law

$$m_p\frac{d\mathbf{u}_p}{dt} = \mathbf{f}_{col,p} + \mathbf{f}_{ext,p}, \quad \text{with} \quad \frac{d\mathbf{x}_p}{dt} = \mathbf{u}_p, \tag{3}$$

where $\mathbf{x}_p$ and $\mathbf{u}_p$ are particle position and velocity, respectively. The total external force $\mathbf{f}_{ext,p}$ includes the gravitational force $\mathbf{f}_{G,p}$ and the forces exerted by the gas phase on the solid phase as the drag $\mathbf{f}_{D,p}$ and the buoyancy $\mathbf{f}_{P,p}$:

$$\mathbf{f}_{ext,p} = \mathbf{f}_{G,p} + \mathbf{f}_{D,p} + \mathbf{f}_{P,p}. \tag{4}$$

The particle rotation is not accounted for in this paper.

The total contact force $\mathbf{f}_{col,p}$ acting on particle p is computed as the sum of all the forces $\mathbf{f}^{col}_{q\to p}$ exerted by the N_p particle and N_w wall contacts:

$$\mathbf{f}_{col,p} = \sum_{b=1}^{N_p+N_w}\mathbf{f}^{col}_{q\to p}. \tag{5}$$

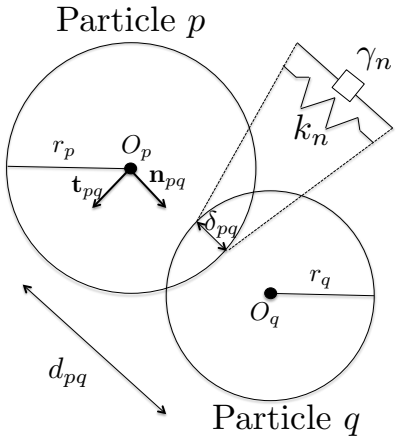

Figure 1: Soft-sphere representation of two particles during collision.

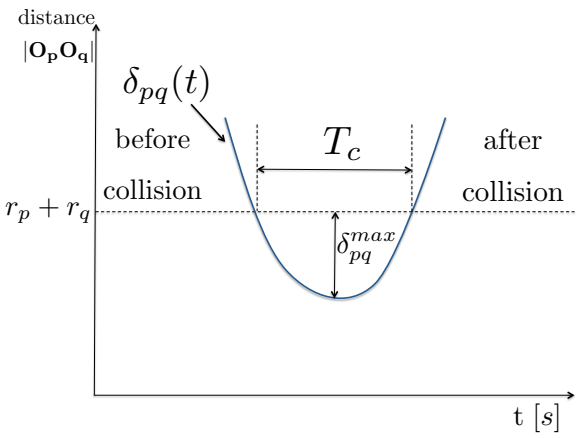

Figure 2: Temporal evolution of a collision between two particles.

As particles and walls are treated similarly during collisions, the q index refers to both. To compute the contact between solid bodies the soft-sphere model is employed. The soft sphere model from Cundall and Strack (1979) is used along with a damped linear-spring and dashpot model to calculate the contact forces. Particles are modeled by a mass-spring-dashpot system (Figure 1). In this frame, the solids are allowed to overlap with each other in a controlled manner and the collision is detected when the distance between two particles and between a particle and a wall is less than the sum of their radii and the radius of the particle, respectively (Figure 1). The overlap δ_{pq} is computed as follows:

$$\delta_{pq} = r_p + r_q - \mid \mathbf{x}_q - \mathbf{x}_p \mid, \tag{6}$$

with r_p and r_q the radii of the particles. The contact forces are divided into normal and tangential contributions:

$$\mathbf{f}_{q\to p}^{col} = \mathbf{f}_{q\to p,n}^{col} + \mathbf{f}_{q\to p,t}^{col}. \tag{7}$$

The normal contribution is modeled by the mass-spring-dashpot equation

$$\mathbf{f}_{q\to p,n}^{col} = \begin{cases} -k_n \delta_{pq} \mathbf{n}_{pq} - 2\gamma_n M_{pq} \mathbf{u}_{pq,n} & \text{if } \delta_{pq} > 0, \\ 0 & \text{otherwise,} \end{cases} \tag{8}$$

where $\mathbf{n}_{pq}$ is the normal unit vector $\mathbf{n}_{pq} = (\mathbf{x}_q - \mathbf{x}_p)/ \mid \mathbf{x}_q - \mathbf{x}_p \mid$, and $\mathbf{u}_{pq,n} = (\mathbf{u}_{pq} \cdot \mathbf{n}_{pq})\mathbf{n}_{pq}$ is the normal component of the relative velocity $\mathbf{u}_{pq} = \mathbf{u}_p - \mathbf{u}_q$. The normal damping parameter γ_n is defined as

$$\gamma_n = \frac{-\ln e_n}{\sqrt{\pi^2 + \ln^2 e_n}} \omega_0, \tag{9}$$

where $\omega_0 = \sqrt{k_n / M_{pq}}$ is the undamped angular frequency based on the stiffness coefficient k_n and the system effective mass $M_{pq} = (1/m_p + 1/m_q)^{-1}$; e_n is the normal restitution coefficient. The tangential contribution is modeled by a Coulomb-type friction law:

$$\mathbf{f}_{q\to p,t}^{col} = -\mu_d \mid \mathbf{f}_{q\to p,n}^{col} \mid \mathbf{t}_{pq}. \tag{10}$$

In Equation (10), the tangential unit vector $\mathbf{t_{pq}}$ is defined on the basis of the tangential relative velocity $\mathbf{u}_{pq,t}$

$$\mathbf{u}_{pq,t} = \mathbf{u}_{pq} - \mathbf{u}_{pq,n}, \quad \mathbf{t}_{pq} = \frac{\mathbf{u}_{pq,t}}{\mid \mathbf{u}_{pq,t} \mid}. \tag{11}$$

For the tangential contribution (Equation (10)), only the Coulomb-type friction is taken into account for both particle-particle and particle-wall collisions, which means that only sliding during collision is considered in order to compare to the "small friction/all sliding" limit case of the TFM numerical simulations. The soft-sphere model requires three user-defined parameters to treat accurately the collisions, which are k_n, e_n and μ_d respectively accounting for the spring stiffness and the particle-particle and particle-wall normal restitution and friction coefficients for the $p-q$ binary system. Hereafter, we will refer to e_c and e_w for the particle-particle and particle-wall normal restitution coefficient, respectively. Accordingly, μ_c and μ_w will refer to the particle-particle and particle-wall friction coefficients, respectively.

2.1.3. Interphase coupling modeling

The effects of the interphase interactions are taken into account in the gas continuity equation (1) and momentum equation (2) through the presence of the gas volume fraction and the particles-to-gas momentum transfer term. The gas-phase variables are interpolated from the Eulerian grid to the particle position ($g@p$) using a trilinear interpolation/projection algorithm on hexahedra. Interpolated velocities should represent the fluid flow undisturbed by the presence of the particle, according to the first-order modeling of the drag (Gatignol (1983); Maxey and Riley (1983)). In a DEM-CFD approach this should be kept in mind when selecting the mesh size. Undisturbed fluid quantities are no longer ensured when the ratio between the mesh size and the particle diameter is not large enough. On the other hand, only resolved fluid fields are seen by the particles in a filtering approach, while sub-grid fluctuations are generally neglected. This is a reasonable assumption only in the presence of large sub-grid Stokes numbers (Fede and Simonin (2006)). Details about the interpolation of Eulerian fields at the p-particle location and projection of the particle contributions onto the Eulerian grid are given in the work of Dufresne et al. (2020). Here, only the interphase coupling term $\mathbf{I}_{p\to g}(\mathbf{x},t)$ is recalled and it is written on each node c as

$$\mathbf{I}_{p\to g}(\mathbf{x}_c,t) = -\frac{1}{\Delta V_c}\sum_{p\in SC_c}\omega_{p,c}(\mathbf{f}_{P,p}+\mathbf{f}_{D,p}), \tag{12}$$

where ΔV_c is the volume of control containing c, $\omega_{p,c}$ is the projection weight, and $p\in SC_c$ stands for all particles belonging to each surrounding cell of node c. In Equation 12, the pressure gradient and drag forces at the particle location are defined as

$$\mathbf{f}_{P,p}(t) = -V_p\nabla P_{g@p} \tag{13}$$

and

$$\mathbf{f}_{D,p}(t) = m_p\frac{\mathbf{u}_{g@p}-\mathbf{u}_p}{\tau_{pg}}, \tag{14}$$

with

$$\tau_{gp} = \frac{4}{3}\frac{\rho_g d_p}{\rho_p C_D|\mathbf{u}_r|} \tag{15}$$

the particle response time and

$$\mathbf{u}_r(t) = \mathbf{u}_{g@p}(t)-\mathbf{u}_p(t) \tag{16}$$

the gas-to-particle relative velocity. Here C_D is the drag coefficient. To take into account the effect of large solid volume fraction, Gobin et al. (2003) proposed the following correlation for the drag coefficient, which is retained in the present work:

$$C_D = \begin{cases} min(C_{D,W\&Y}, C_{D,E}), & \text{if } \alpha_g < 0.7 \\ C_{D,W\&Y}, & \text{otherwise} \end{cases} \tag{17}$$

where $C_{D,W\&Y}$, and $C_{D,E}$ are Wen and Yu (1966) and Ergun (1952) correlations, respectively,

$$C_{D,W\&Y} = \begin{cases} \frac{24}{Re_p}(1 + 0.15Re_p^{0.687})\alpha_g^{-1.7}, & \text{for } Re_p < 1000 \\ 0.44\alpha_g^{-1.7}, & \text{otherwise} \end{cases} \tag{18}$$

$$C_{D,E} = 200\frac{1-\alpha_g}{Re_p} + \frac{7}{3} \tag{19}$$

and Re_p the particle Reynolds number defined as

$$Re_p = \alpha_g \frac{\rho_g |\mathbf{u}_r| d_p}{\mu_g}. \tag{20}$$

2.1.4. Time step criteria

The fluid is advanced in time by a time step, Δt_f, which is computed during the simulation using classical CFL criteria. The characteristics of the particles are computed at $t_f + \Delta t_f$ from the resolution of the particle trajectory equations, coupled through the soft-sphere collision model, by a sub-step method between t_f and $t_f + \Delta t_f$. During this time step Δt_f, the fluid is frozen at t_f and particles advanced in time by a time step $\Delta t_p < \Delta t_f$. The time step Δt_p of the last sub-step is computed such that the sum of time steps is equal to Δt_f. Source terms are updated at the end of each particle sub-step. After all particle sub-steps have been computed, the source terms are accounted for on the Eulerian grid. The fluid flow is then computed at $t_f + \Delta t_f$ using the prediction-correction algorithm.

The choice of Δt_p is subject to conditions ensuring that collisions are treated appropriately. In the frame of the soft-sphere model, the first condition concerns the contact duration, T_c, which is written as:

$$T_c = \frac{\pi}{\sqrt{\omega_0^2 - \gamma_n^2}}. \tag{21}$$

Since particles are identical in our simulations, T_c has a unique value in the particulate phase. According to Eq. (21), the contact duration depends on ω_0 and γ_n, which depend on k_n, and on e_n and the particles properties. It is important to note that, in the frame of the soft-sphere model, k_n is not a physical but rather a numerical parameter. Indeed, the true physical value of k_n imposed by the particle deformation properties leads in general to a much too small value of T_c corresponding to nearly hard sphere collision. So, the DEM-CFD approach is generally using a smaller value of k_n, corresponding to more deformable particles but without measurable effect on the particle statistics. A way to select an appropriate value of k_n is to estimate it beforehand on the basis of the mean value of the normal relative velocity at the first impact, and the overlap constraint ($\delta_{max}/d_p < 0.1$). Accordingly, a stiffness coefficient value of 300 N/m was found; this value was used for all the numerical simulations (Nigmetova et al. (2021)).

The second condition ensures that the particle time step, Δt_p, is smaller than the contact time, T_c, in order to limit the overlap distance during the collision and to reach a sufficient resolution for the time integration of stiff collisions (see Figure 2). The particle time step should verify the following relationship:

$$\Delta t_p < \frac{T_c}{N_c}, \tag{22}$$

where N_c is the needed number of sub-steps during one contact to insure satisfactory inter-particle collision prediction. According to van der Hoef et al. (2006), the step number should be $N_c > 5$. The latter also depends on the choice of the numerical scheme. Preliminary tests have shown that a value of $N_c \geq 10$ is recommended in order to provide accurate solutions. Accordingly, $N_c = 10$ was finally retained in the present work.

Additional CFL conditions are introduced. They are needed when the ratio between the running time of the particles and the contact duration increases, which may occur in the dilute regions of the bed. The first one impose that $\Delta t_p \leq CFL_p \times \Delta x/|\mathbf{u}_p|$ to ensure that a particle does not move more than few elements of the Eulerian mesh during a sub-step. The second condition requires that during a sub-step particles do not move more than $100 \cdot CFL_p^{col}$ % of their diameter, that is $\Delta t_p \leq CFL_p^{col} \times d_p/|\mathbf{u}_{rn}^0|$, where $\mathbf{u}_{rn}^0$ is the relative particle-particle velocity at the instant when the first overlap between the particles is detected. The latter condition is necessary to control and limit the overlapping distance at the initial detection of the impact. Finally, Δt_p is checked to be smaller then the particle relaxation time τ_{pg}. The minimum of all the aforementioned conditions for all the particles is computed at the beginning of each particle step in order to define Δt_p. In the present work, the following parameters were chosen: $CFL_p = 1.5$, $CFL_p^{col} = 0.3$ and $CFL_f = 0.1$.

2.2. Eulerian particle fields

2.2.1. Post-processing: projected Eulerian particle fields from DEM predictions

To extract instantaneous Eulerian particle fields from Lagrangian data, DEM-CFD results are post-processed during the numerical simulation using a projection operator. The Eulerian particle velocity $\widehat{\mathbf{u}}_p$ is computed on a distribution of fixed points $\mathbf{x}_c$, which correspond to the centers of cubic cells of volume V_c. The Eulerian particle field at $\mathbf{x}_c$ is obtained as follows:

$$\widehat{n}_p(\mathbf{x}_c, t)\widehat{\mathbf{u}}_p(\mathbf{x}_c, t) = \frac{1}{V_c}\sum_{n=1}^{N_p} \phi_c(\mathbf{x}_p^{(n)}(t))\mathbf{u}_p^{(n)}(t). \tag{23}$$

In Equation (23), $\widehat{n}_p$ is the particle number density given by

$$\widehat{n}_p(\mathbf{x}_c, t) = \frac{1}{V_c}\sum_{n=1}^{N_p} \phi_c(\mathbf{x}_p^{(n)}(t)), \tag{24}$$

and ϕ_c is a weight defined as

$$\phi_c(\mathbf{x}_p^{(n)}(t)) = \begin{cases} 1, & \text{if } \mathbf{x}_p^{(n)}(t) \in V_c \\ 0, & \text{otherwise} \end{cases} . \tag{25}$$

Therefore, any Lagrangian n-particle ($n \in (1, N_p)$) instantaneous velocity can be decomposed in two contributions:

$$\mathbf{u}_p^{(n)}(t) = \widehat{\mathbf{u}}_p(\mathbf{x}_p^{(n)}(t), t) + \delta\mathbf{u}_p^{(n)}(t). \tag{26}$$

The first contribution is the interpolation of the Eulerian particle velocity $\widehat{\mathbf{u}}_p$ at the particle center position, the second contribution, $\delta\mathbf{u}_p^{(n)}(t)$, represents the deviation of the Lagrangian n-particle velocity from the interpolated Eulerian field. The interpolation of the Eulerian particle velocity field at the particle center position is written as

$$\widehat{\mathbf{u}}_p(\mathbf{x}_p{}^{(n)}(t), t) = \sum_{c=1}^{N_c} \phi_c(\mathbf{x}_p^{(n)}(t))\widehat{\mathbf{u}}_p(\mathbf{x}_c, t), \tag{27}$$

According to the choice of the projection/interpolation operator, the idempotency is satisfied :

$$\widehat{\widehat{\mathbf{u}}}_p(\mathbf{x}_c, t) = \frac{1}{V_c}\frac{\sum_{n=1}^{N_p} \phi_c(\mathbf{x}_p^{(n)}(t))\widehat{\mathbf{u}}_p(\mathbf{x}_p^{(n)}(t), t)}{\widehat{n}_p(\mathbf{x}_c, t)} = \widehat{\mathbf{u}}_p(\mathbf{x}_c, t), \tag{28}$$

$$\widehat{\delta\mathbf{u}_p}(\mathbf{x}_c, t) = \frac{1}{V_c}\frac{\sum_{n=1}^{N_p} \phi_c(\mathbf{x}_p^{(n)}(t))\delta\mathbf{u}_p^{(n)}(t)}{\widehat{n}_p(\mathbf{x}_c, t)} = 0. \tag{29}$$

As shown by Figure 3, the projection cells are cubic elements of Cartesian-radial meshes, all of same volume $V_c = {\Delta x_c}^3$. Each Cartesian-radial mesh is defined by cell centers $\mathbf{x}_c$ distributed, from $r_c = 0$ to $r_c = R$, by a constant interval Δx_c, along a radius defined by an angle θ_c on a horizontal plane at z_c. To cover the whole domain, the angle θ_c is varying from 0 to 2π by an uniform angle increment $\Delta\theta_c = 2\pi/71 (= 5°)$. Thus, at a given height z_c, 71 different radial profiles of the instantaneous particle Eulerian fields are computed from the DEM-CFD Lagrangian simulation.

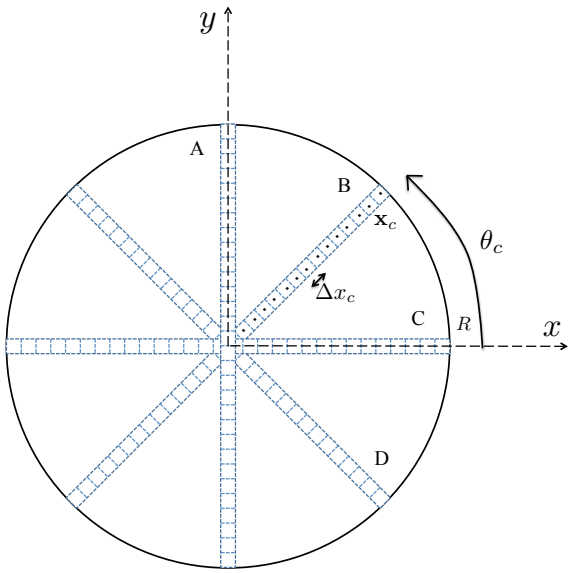

Figure 3: Cartesian-radial mesh: R is the cylinder radius, Δx_c is the projection mesh size.

From the instantaneous particle Eulerian fields, averaged quantities can be extracted from the numerical simulation. For example, from $\widehat{n}_p(\mathbf{x}_c, t)$ the time-averaged solid volume fraction and the variance of the solid volume fraction can be defined at each $\mathbf{x}_c$. The former is computed as follows:

$$\overline{\alpha}_p(\mathbf{x}_c) = V_p \overline{\widehat{n}}_p(\mathbf{x}_c) = \frac{\sum_{k=1}^{N_t} V_p \widehat{n}_p(\mathbf{x}_c, t_k)\Delta t_k}{\sum_{k=1}^{N_t} \Delta t_k}. \tag{30}$$

In Equation (30) Δt_k is the DEM-CFD computational time step at time t_k, and V_p is the particle volume. The variance of the solid volume fraction is then obtained as follows:

$$\overline{{\alpha'_p}^2}(\mathbf{x}_c) = \frac{\sum_{k=1}^{N_t} (V_p \widehat{n}_p(\mathbf{x}_c, t_k) - \overline{\alpha}_p(\mathbf{x}_c))^2 \Delta t_k}{\sum_{k=1}^{N_t} \Delta t_k}. \tag{31}$$

Similarly, the time-averaged Eulerian particle velocity is computed as

$$\mathbf{U}_p(\mathbf{x}_c) = \overline{\widehat{\mathbf{u}}}_p(\mathbf{x_c}) = \frac{\sum_{k=1}^{N_t} \widehat{n}_p(\mathbf{x}_c, t_k)\widehat{\mathbf{u}}_p(\mathbf{x}_c, t_k)\Delta t_k}{\sum_{k=1}^{N_t} \widehat{n}_p(\mathbf{x}_c, t_k)\Delta t_k}. \tag{32}$$

From the latter, the fluctuation of the projected Eulerian particle velocity is defined,

$$\widehat{\mathbf{u}}'_p(\mathbf{x}_c,t) = \widehat{\mathbf{u}}_p(\mathbf{x}_c,t) - \mathbf{U}_p(\mathbf{x}_c), \tag{33}$$

and the second-order correlation of the projected Eulerian particle velocity is obtained

$$\overline{\widehat{u}'_{p,i}\widehat{u}'_{p,j}}(\mathbf{x}_c) = \frac{\displaystyle\sum_{k=1}^{N_t} \widehat{n}_p(\mathbf{x}_c,t_k)\widehat{u}_{p,i}(\mathbf{x}_c,t_k)\widehat{u}_{p,j}(\mathbf{x}_c,t_k)\Delta t_k}{\displaystyle\sum_{k=1}^{N_t} \widehat{n}_p(\mathbf{x}_c,t_k)\Delta t_k} - U_{p,i}(\mathbf{x}_c)U_{p,j}(\mathbf{x}_c). \tag{34}$$

A Lagrangian fluctuation of the total particle velocity $\mathbf{u}_p^{(n)}(t)$ is also defined as follows:

$$\mathbf{u}_p{}'^{(n)}(t) = \mathbf{u}_p{}^{(n)}(t) - \mathbf{U}_p(\mathbf{x}_p{}^{(n)}(t)), \tag{35}$$

where $\mathbf{U}_p(\mathbf{x}_p{}^{(n)}(t))$ is the Lagrangian average particle velocity obtained by the interpolation of the time-averaged Eulerian particle velocity at the particle center position:

$$\mathbf{U}_p(\mathbf{x}_p{}^{(n)}(t)) = \sum_{c=1}^{N_c} \phi_c(\mathbf{x}_p^{(n)}(t))\mathbf{U}_p(\mathbf{x}_c). \tag{36}$$

Therefore, a time-averaged second-order correlation of the Lagrangian particle velocity $\mathbf{u}_p^{(n)}$ may be written as follows:

$$\overline{u'_{p,i}u'_{p,j}}(\mathbf{x}_c) = \frac{\displaystyle\sum_{k=1}^{N_t} \widehat{n}_p(\mathbf{x}_c,t_k)\widehat{\overline{u_{p,i}u_{p,j}}}(\mathbf{x}_c,t_k)\Delta t_k}{\displaystyle\sum_{k=1}^{N_t} \widehat{n}_p(\mathbf{x}_c,t_k)\Delta t_k} - U_{p,i}(\mathbf{x}_c)U_{p,j}(\mathbf{x}_c). \tag{37}$$

In addition, the second-order moment of the Lagrangian velocity deviation $\delta u_p^{(n)}(t)$ may be defined as

$$\overline{\delta u_{p,i}\delta u_{p,j}}(\mathbf{x}_c) = \frac{\displaystyle\sum_{k=1}^{N_t} \widehat{n}_p(\mathbf{x}_c,t_k)\widehat{\overline{\delta u_{p,i}\delta u_{p,j}}}(\mathbf{x}_c,t)\Delta t_k}{\displaystyle\sum_{k=1}^{N_t} \widehat{n}_p(\mathbf{x}_c,t_k)\Delta t_k}. \tag{38}$$

By construction, according to the idempotency of the joint projection-interpolation operator, the following relation applies :

$$\overline{\delta u_{p,i}\delta u_{p,j}}(\mathbf{x}_c) = \overline{u'_{p,i}u'_{p,j}}(\mathbf{x}_c) - \overline{\widehat{u}'_{p,i}\widehat{u}'_{p,j}}(\mathbf{x}_c). \tag{39}$$

Let us introduce an angle-averaging operator $\{\cdot\}$ corresponding to the arithmetic mean over all the angles, for a given value of r_c and z_c. For all quantities other than the solid volume fraction and its moments, the time-averaged particle number density is used as a weight. For example, the angle-average of the time-averaged Eulerian particle velocity is written as:

$$\{\overline{\widehat{\mathbf{u}}}_p\}(r_c,z_c) = \frac{\displaystyle\sum_{m=1}^{71} \overline{\widehat{\mathbf{u}}}_p(r_c,\theta_c^{(m)},z_c)\overline{\widehat{n}}_p(r_c,\theta_c^{(m)},z_c)}{\displaystyle\sum_{m=1}^{71} \overline{\widehat{n}}_p(r_c,\theta_c^{(m)},z_c)}. \tag{40}$$

It should be mentioned that the introduction of a Cartesian-radial mesh was needed to provide radial profiles of particle time-averaged Eulerian fields in such a cylindrical configuration. However, angle-time-averaged quantities are in excellent agreement with the spatial-time-averaged quantities obtained on the cylindrical mesh over toroids of vertical section $\delta x_c \times \delta x_c$, centered on the cylinder axis at z_c, as expected by construction.

2.2.2. Eulerian particle fields in the frame of the TFM approach

According to the Mesoscopic Eulerian Formalism introduced by Février et al. (2005), the particle Lagrangian velocity may be separated in two components which obey the following decomposition:

$$\mathbf{u}_p^{(n)}(t) = \widetilde{\mathbf{u}}_p(\mathbf{x}_p^{(n)}(t), t) + \delta\mathbf{u}_p^{(n)}(t). \tag{41}$$

The first contribution represents the interpolation at the particle position of an Eulerian correlated velocity field $\widetilde{u}_p$, shared by all the particles, which corresponds to the Eulerian resolved part of the particle velocity in the frame of a TFM approach (Fox (2014)). The second contribution is a random spatially-uncorrelated Lagrangian velocity distribution along the particle paths, referred to as Random Uncorrelated Motion (RUM). The latter is due to the particle inertia which may lead two close particles to have considerably different velocities, which means that their velocities may be uncorrelated even when the distance between them is very small (Ijzermans et al. (2010)).

In very dilute flows, the effect of the RUM on the resolved velocity prediction is mainly accounted for through the modeling of the particle shear stresses (Simonin et al. (2002); Vance et al. (2006); Kaufmann et al. (2008); Moreau et al. (2010); Masi et al. (2014); Vié et al. (2015)). In the frame of the TFM approach for dense flows, the effect of the RUM relies on the modeling of the particle-particle and particle-wall collisions and of the particle pressure and shear stress by using the kinetic theory of granular flow (KTGF) (see, for example, Gidaspow (1994)). In this work, we compare the DEM-CFD time-averaged results with the corresponding TFM time-averaged predictions obtained by Fede et al. (2016). In their approach, the authors used a separate transport equation for the RUM kinetic energy. The latter is theoretically defined as half of the variance of the RUM contribution in an Eulerian framework (δq_p^2). It is related to the particle granular temperature (Θ_p), more commonly used in the literature, by the following relationship: $\Theta_p = 2/3\delta q_p^2$. In the work of Fede et al. (2016), in addition to inter-particle collision effect, modeled viscosity and RUM kinetic-energy diffusivity are accounting for the effect of the friction by the interstitial gas.

Moments of the RUM particle velocity contribution (i.e. RUM kinetic energy, RUM velocity stress tensor, etc.) obtained by an Eulerian approach (as TFM) are based on the modeling used to close the system of equations in an Eulerian framework. Their correspondence with the theoretical values depends on the modeled closures, as well as their accuracy on the numerical methods. Such moments extracted by a Lagrangian simulation (as DEM) owe instead their representativeness on the choice of the post-processing projection/interpolation algorithm as well as on the local and instantaneous particle sample to ensure statistical convergence (the reader is referred to the works of Moreau et al. (2010) and Kaufmann et al. (2008) for more details). The algorithm used in this work (Section 2.2.1) to extract the Eulerian particle velocity ($\widehat{\mathbf{u}}_p$), as well as the Lagrangian particle velocity deviation ($\delta\mathbf{u}_p^{(n)}(t)$) from such an interpolated Eulerian field, is one of the most simple. It has the advantage of being idempotent with respect to the interpolation and projection operations, but it assumes a null particle velocity gradient in the projection/interpolation volume of control. This approximation is acceptable in dense suspension where collisions act at reducing the local mean shear. However, it should kept in mind when analyzing time-averaged Eulerian particle second order moments extracted by the

DEM-CFD numerical simulations. Low order moments (as the time-averaged particle velocity) are indeed not affected by such an approximation, being the mean particle velocity equal by construction regardless of whether it is obtained, by Lagrangian or projected particle velocity. Even if aware of the limits of such an estimation method for high order moments, hereafter, for a matter of simplicity, we will refer to correlated and RUM contributions for, respectively, the moments of the projected particle velocity and the moments of its complementary contribution to the Lagrangian total one computed in an Eulerian framework.

3. Numerical simulations

The test case is a pressurized gas-solid fluidized bed, for which experimental data are available from the literature (Fede et al. (2009)). Numerical simulations are performed using YALES2. The goal of the numerical simulation is to reproduce the fluidized bed at mesoscopic scale in order to improve the knowledge of the local and instantaneous particulate behavior inside the bed, such to provide information to use in macroscopic (Eulerian) modeling.

3.1. Experiments and available measurements

Experiments of an isothermal pressurized gas-solid fluidized bed were reproduced in laboratory at the University of Birmingham. The pilot consists of a cylindrical reactor of internal radius $R = 77$ mm and height 1074 mm (including the enlargement zone). For the operating point retained in the present study, the bed is filled with 2.5 kg of solid particles of mean diameter $d_p = 875$ μm and density $\rho_p = 740$ kg/m^3, which corresponds to about 10 million spherical particles. Particles are fluidized by nitrogen injected at 0.32 m/s, at the operating conditions of 12 bar and 298 K. A such pressure and temperature the gas density and viscosity are, respectively, $\rho_g = 13.595$ kg/m^3 and $\mu_g = 1.7982 \times 10^{-5}$ Pa s. In such experiments, PEPT was used to extract information about the motion of the solid in the fluidized bed. This technique, developed at the Positron Imaging Centre of the University of Birmingham (Seville et al. (2005); Parker et al. (2008)), makes indeed it possible to track a marked particle inside the bed and to reconstruct, by post-processing the particle position, the mean, toroidal spatial-time averaged, particle velocity at different locations (r_c, z_c). Further detailed about the experiments may be found in the work of Fede et al. (2009). In such a work, the authors studied the influence of the acquisition time step and of the cell size on the representativity of the mean particle velocity, also estimating a statistical error based on the number of events. This made it possible to recover the experimental profiles of the mean vertical particle velocity at different heights. However, because of the very small number of events at the freeboard, the bed height could not be measured experimentally.

3.2. Collision parameters

The physical parameters available from the experiments (and recalled in Section 3.1) are used in the numerical simulations as well. However, additional specifications are needed to perform the numerical simulations using a DEM approach. Foerster et al. (1994) showed that an accurate choice of three constant parameters enables to capture the behavior of the particle-particle and/or particle-wall collisions. These parameters are the Coulomb friction and the normal and tangential restitution coefficients. The first one accounts for the dynamic friction between solids (particle-particle or particle-wall) in sliding conditions. The second and third coefficients account for dissipation and deformation due to inelastic and elastic collisions, respectively. The choice of such parameters in the DEM-CFD simulations is dictated by the objective of the present study which is twofold: i) to gain insight in the physics of the bed at

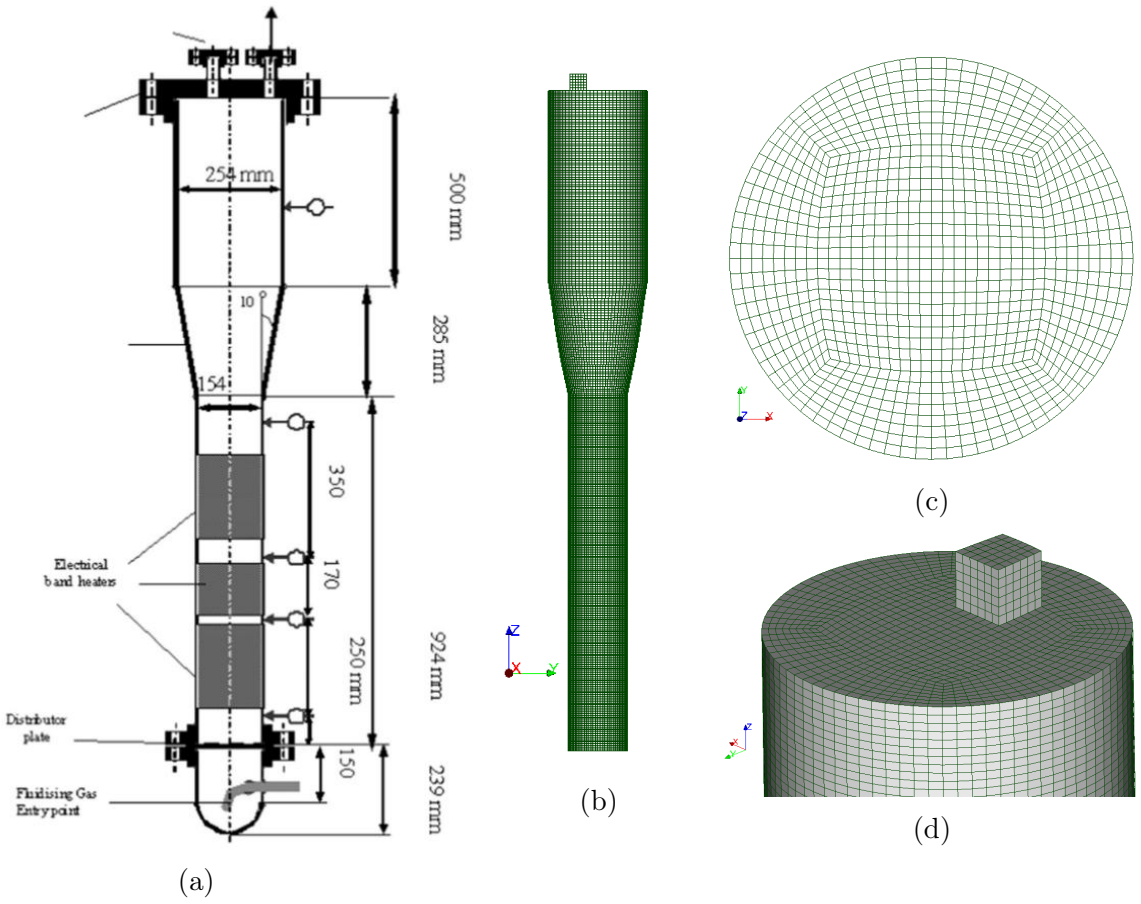

Figure 4: Bed reactor: experimental sketch (a) excerpted from Fede et al. (2016) and numerical geometry: front view (b), bottom view (c), top view (d). The mesh corresponds to 349 656 hexahedra of size $\Delta x \simeq 5d_p$.

mesoscopic scale; ii) to provide information for macroscopic modeling. In this regard, DEM-CFD results are compared with numerical results available from the literature obtained by a TFM approach (Fede et al. (2016)). For this reason, the same collision parameters as the TFM simulations are used as a reference. For example, as mentioned in section Section 2.1.2, we assumed that collisions only occur with sliding during the contact. Under such an assumption, only two parameters need to be specified to model collisions, which are the Coulomb friction, μ_d, and the normal restitution coefficient, e_n, both for particle-particle and particle-wall collisions. Together with the normal spring stiffness coefficient k_n (which is an additional parameter required in the soft-sphere model), they define a set of five values to be selected in the numerical simulation. Three of them are fixed for all the simulations. They are the normal spring stiffness coefficient (whose choice, $k_n = 300$ N/m, was explained in Section 2.1.4), the Coulomb friction corresponding to the particle-particle collision ($\mu_c = 0$, as in the TFM simulations) and the normal particle-wall restitution coefficient ($e_w = 1$). Concerning the latter, Fede et al. (2016) showed that its effect is negligible on the mean particle vertical velocity and the bed height, this is why only one value is retained in the present study. The other two parameters are made to vary for an analysis purpose.

3.3. Simulation conditions

For the numerical simulations, a simplified geometry is used. The simplified reactor is meshed using the O-grid technique in order to have nearly uniform cells in each horizontal section. Figure 4 shows the original experimental sketch (a) and the numerical geometry (front

Parameters	RUN-I	RUN-II	RUN-III	RUN-IV	RUN-V
e_c	0.9	0.9	0.8	1	0.9
μ_w	0	0	0	0	0.3
Δx	$5dp$	$3dp$	$5dp$	$5dp$	$5dp$
Physical time [s]	70	40	33	56	60
Time for statistics (time averages) [s]	27	20	15	16	20
Wall-clock time [days]	155	95	75	75	145
CPU time [h]	1 249 920	893 760	604 800	604 800	1 169 280

Table 1: Test cases and corresponding numerical parameters.

(b), bottom (c) and top (d) mesh views). The distribution plate is simulated as an uniform inlet for the gas and as a wall for the particles. The chimney located at the top of the reactor is a free outlet both for the gas and the particles (even if no particle leaves the bed during the simulation). Due to the relatively low mean particle Reynolds number ($\mathrm{Re}_p = 212$) the gas is considered as laminar and no sub-grid scale model is used. This choice is also motivated by the need to reproduce the TFM numerical simulations in which a laminar gas assumption was considered. Accordingly, no-slip boundary conditions are used for the gas.

First, the effect of the simulation mesh size on the numerical predictions is studied using the DEM-CFD approach. Two grids of mesh size $\Delta x \simeq \Delta y \simeq \Delta z \simeq 5d_p$, $3d_p$ (RUN-I, RUN-II) are investigated. They correspond to a number of mesh cells 349 656 and 1 411 664, respectively. This analysis is realized for the reference case corresponding to $e_c = 0.9$, $\mu_c = 0$ and $e_w = 1$, $\mu_w = 0$. Next, different particle-particle normal restitution coefficients ($e_c = 0.8$, 0.9, 1) are investigated in order to analyze their impact on the hydrodynamics of the fluidized bed (RUN-III, RUN-I, RUN-IV). Further, two different particle-wall friction coefficients ($\mu_w = 0$, 0.3) are analyzed in order to study the effect of the friction with the wall comparing with experimental results for the mean particle vertical velocity (RUN-I, RUN-V). A summary of the numerical parameters and test cases is given in Table 1. The physical time for each simulation is also given together with the CPU time. The latter also accounts for the cost of post-processing which is carried out during the numerical simulation at each time step in order to obtain projected particle fields and related deviations (particle moments).

4. Results and discussion

In this section, the DEM-CFD predictions are presented and analyzed. Comparisons with the experimental results will be discussed at the same time than those with the TFM predictions because most of the choices undertaken in selecting collision parameters were supported by the intent to compare mesoscopic (DEM-CFD) and macroscopic (TFM) modeling predictions before getting into the physical aspects of the analysis.

Before presenting the different DEM-CFD predictions, a preliminary analysis is carried out on the sensitivity of the particle Eulerian fields, obtained from Lagrangian data, on the post-processing mesh size. This analysis is presented in Section 4.1 and should not be confused with the aforementioned analysis on the effect of the simulation mesh size which is presented in Section 4.2.

4.1. Sensitivity on the post-processing mesh size

The time-averaged quantities are calculated on $m(\in [1, 71])$ different radial profiles and then averaged over all the profiles to represent a toroidal spatial average, allowing comparison

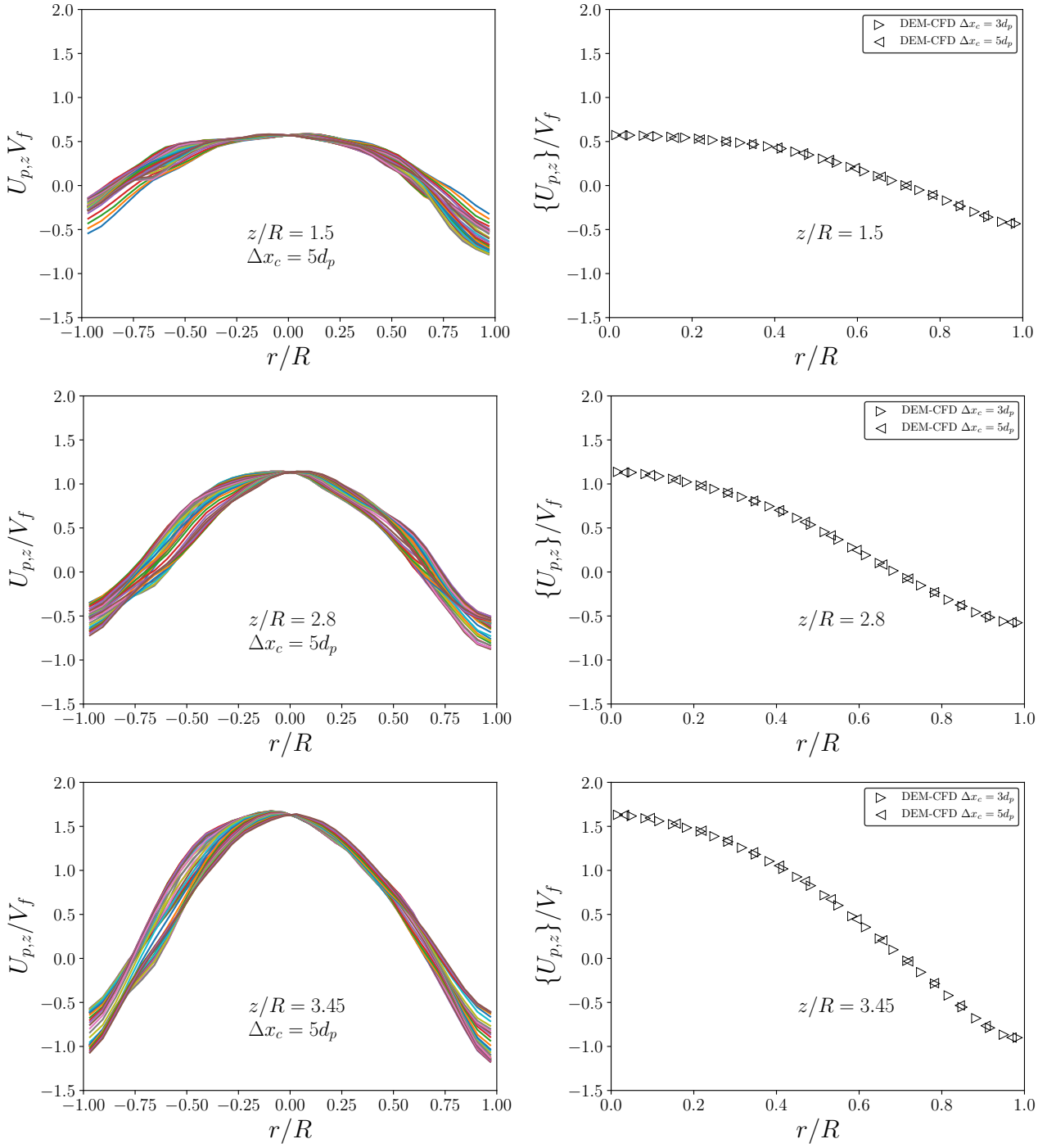

Figure 5: Radial profiles of the time-averaged (left) and angle-time-averaged (right) projected vertical particle velocities (RUN-I). Sensitivity on the projection mesh size (right).

with the experimental data and TFM results. According to the large running time used by Fede et al. (2016) in their numerical simulations, the duration of the DEM-CFD simulations is probably not sufficient to allow time-averaged quantities to converge towards axisymmetric fields. As we can observe by Figure 5 (left) and Figure 6 (left), the m radial profiles of the time-averaged particle velocity and the time-averaged variance of the vertical total particle velocity exhibit a spatial dispersion. However, such a dispersion is small compared to the value of the variance itself (Figure 6 (left)), which means that the essential of the angle-time-averaged variance (Figure 6 (right)) is related to the temporal fluctuations and not to the

non-axisymmetry of the measured radial profiles. We assume that the spatio-temporal average converges more quickly over time; this is why it is used to compare DEM-CFD results with experimental results or with predictions obtained using the TFM approach.

To study the effect of the projection mesh, two mesh sizes are investigated: $\Delta x_c = 3d_p$ and $5d_p$ (to not be confused with the simulation mesh size, Δx, which is analyzed in the next section). The question arises because the choice of the mesh size is not trivial. On the one hand a small cell may not ensure statistically representative fields because of the insufficient number of events. On the other hand a larger cell may lead to mitigate the effects of the smallest scales, therefore reducing the particle velocity fluctuations due to the correlated contribution (Kaufmann et al. (2008); Moreau et al. (2010)). Figure 5 (right) and Figure 6 (right) show that the two mesh sizes here investigated give almost identical results for both projected vertical particle velocity and vertical total particle velocity variance.

4.2. Sensitivity on the numerical simulation mesh size

The coupling between the particles and the gas phase is performed explicitly through the inter-phase coupling quantities (forces and volume fractions) by means of the trilinear interpolation/projection algorithms, whose accuracy depends on the grid size compared to the particle diameter. On the one hand, a DEM-CFD approach should ensure that the Eulerian grid size is large enough to comply with the scale separation. In a DEM-CFD framework, this criterion is consistent with the modeling of the fluid (accounting for the particulate phase), whose equations are defined over a scale larger than the particle size by means of a spatial-average operator. On the other hand, the smaller is the Eulerian grid size the more accurate is the fluid resolution. It is clear that these two assumptions may not be held at once. According to Pepiot and Desjardins (2012), the control volume should be at least an order magnitude larger than the particle one, therefore indicating a grid of mesh size $\Delta x \simeq 1.74d_p$ as the finest admitted. Moreover, they pointed out as a large particle diameter compared to the mesh size may produce numerical instabilities because of the oscillations appearing in the results of the projection operation onto the Eulerian grid. In their work, Pepiot and Desjardins (2012) used a mollification approach to extrapolate Lagrangian data onto the Eulerian mesh. In simulating a fluidized bed, they finally used $\Delta x \simeq 1.86d_p$ as a grid size. Link et al. (2005) pointed out that a volume of control of size corresponding to 3-5 times d_p is generally used in a DEM-CFD approach. In their work the authors proposed and used an alternative way to compute inter-phase coupling by means of porous cubes representing the particles and allowing to overlap. In their study on a pseudo-2D spout-fluid bed configuration, the authors found nearly identical predictions using a grid size of about $2d_p$ and $4d_p$, respectively. Bernard et al. (2016) studied the effect of the mesh size on a biperiodic fluidized bed. In their approach, the authors modeled the projection of each drag-force components (because of the staggered grid) by means of a projection operator based on the solid fraction estimated in the volume of control by the method of Link et al. (2005). They claimed almost mesh-independent results for $1.85d_p \leq \Delta x \leq 2.5d_p$, finally retaining $\Delta x = 2d_p$ for their numerical simulations.

The choice of the mesh size clearly depends on the algorithms used in the DEM-CFD approach, and it can be expected to be case sensitive as well. To select a grid size representing the best compromise between the two aforementioned requirements, a preliminary study was first carried out. Such a study was conducted using a simplified configuration, corresponding to an array of fixed particles randomly distributed. Particle and fluid properties and operating conditions were chosen the same as the pressurized fluidized bed. Results (here not shown) suggested a grid of mesh size corresponding to $\Delta x \simeq 3d_p$, using the algorithms described in Section 2.1.3. However, the use of a coarser mesh would reduce the computational costs. A

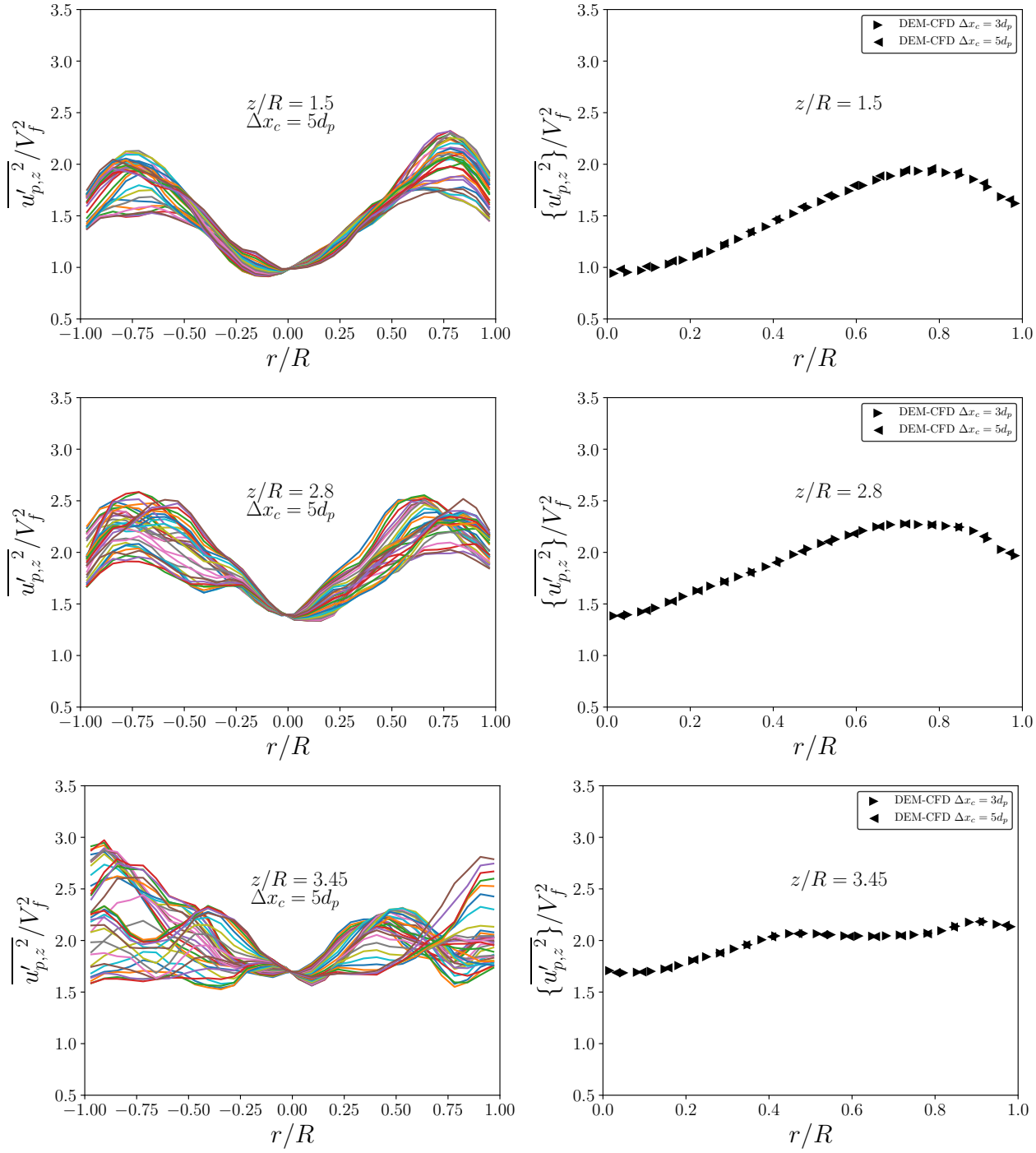

Figure 6: Radial profiles of the time-averaged (left) and angle-time-averaged (right) variance of the total vertical particle velocity (RUN-I). Sensitivity on the projection mesh size (right).

preliminary analysis was therefore carried out with the scope to investigate the suitability of the use of a larger mesh size in the fluidized bed configuration. Two numerical simulations using, respectively, $\Delta x \simeq 5d_p$ (RUN-I) and $\Delta x \simeq 3d_p$ (RUN-II) were performed, and results compared. Figure 7(left) shows the vertical profiles of the mean (time-averaged) relative pressure for the two test cases. No appreciable difference is detected. The two grid sizes predict the same bed height. Differences are instead observed on the time-averaged solid fraction, displayed in Figure 7(right). The latter compares radial profiles at one selected vertical location. Figure shows that the coarsest grid yields larger particle volume fraction than the finest mesh. This

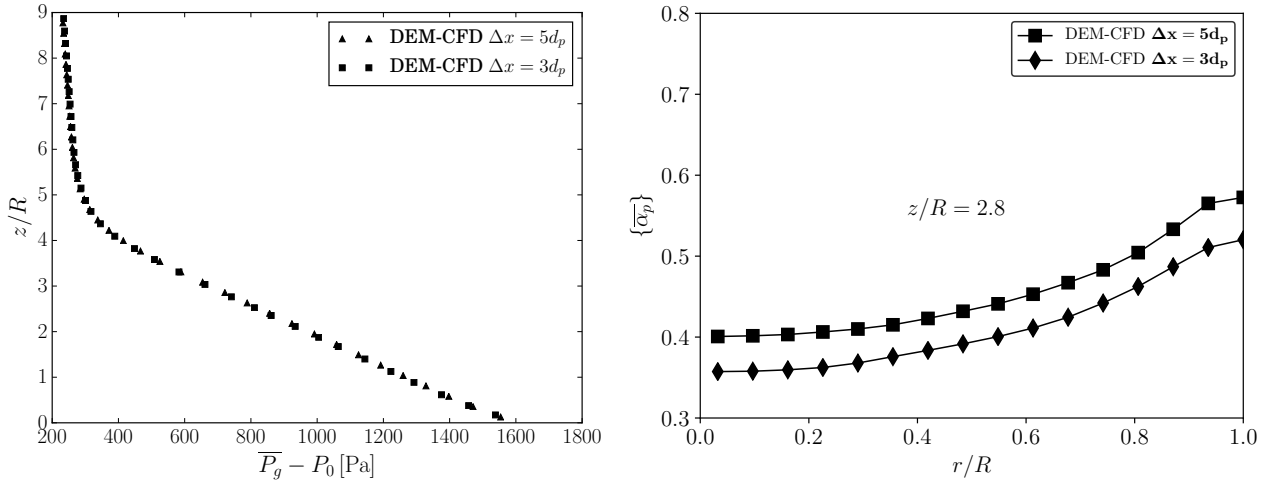

Figure 7: Vertical profile of the time-averaged gas pressure at the wall (left) and radial profiles of the angle-time-averaged solid volume fraction at a selected reactor station (right). Sensitivity on the simulation mesh size Δx.

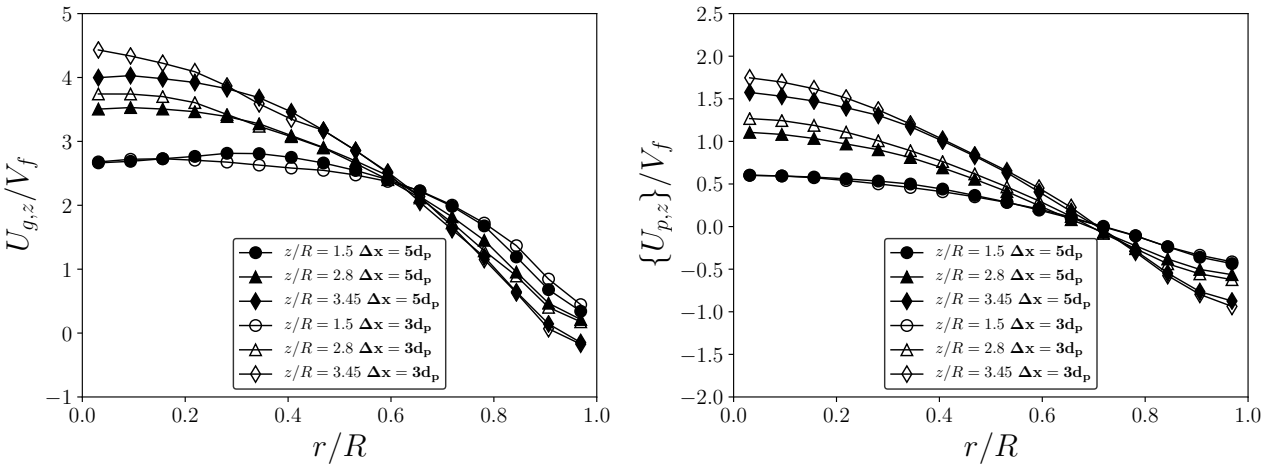

Figure 8: Radial profiles of the spatial-time-averaged vertical gas velocity (left) and of the angle-time-averaged vertical particle velocity (right). Sensitivity on the simulation mesh size Δx.

difference is imperceptible in terms of pressure drop (a few dozen Pascals). Finally, the influence of the mesh size on the gas and particle velocity is analyzed. Radial profiles of the spatial-time-averaged vertical gas velocity and the angle-time-averaged vertical particle velocity are computed and depicted in Figure 8, at different heights. Close to the inlet ($z/R = 1.5$, where R is the reactor internal radius), predictions are very similar both at the center and near the wall. At higher locations ($z/R = 2.8, 3.45$), velocities obtained using the coarsest mesh exhibit lower values at the reactor center, while very similar predictions are found close to the wall.

In the present study, we mainly focus on the particulate phase behavior near the wall with the intent to improve the understanding of some physical mechanisms observed in the experiments. Such an understanding is essential to allow the formulation of appropriate boundary conditions in macroscopic modeling. On the basis of the results obtained with $\Delta x \simeq 5d_p$ near the wall, we concluded that such a refinement is a good compromise also accounting for computational cost issues. This choice is also supported by the fact that $\Delta x \simeq 5d_p$ was used in the TFM simulations as well. This is why such a mesh size was finally retained.

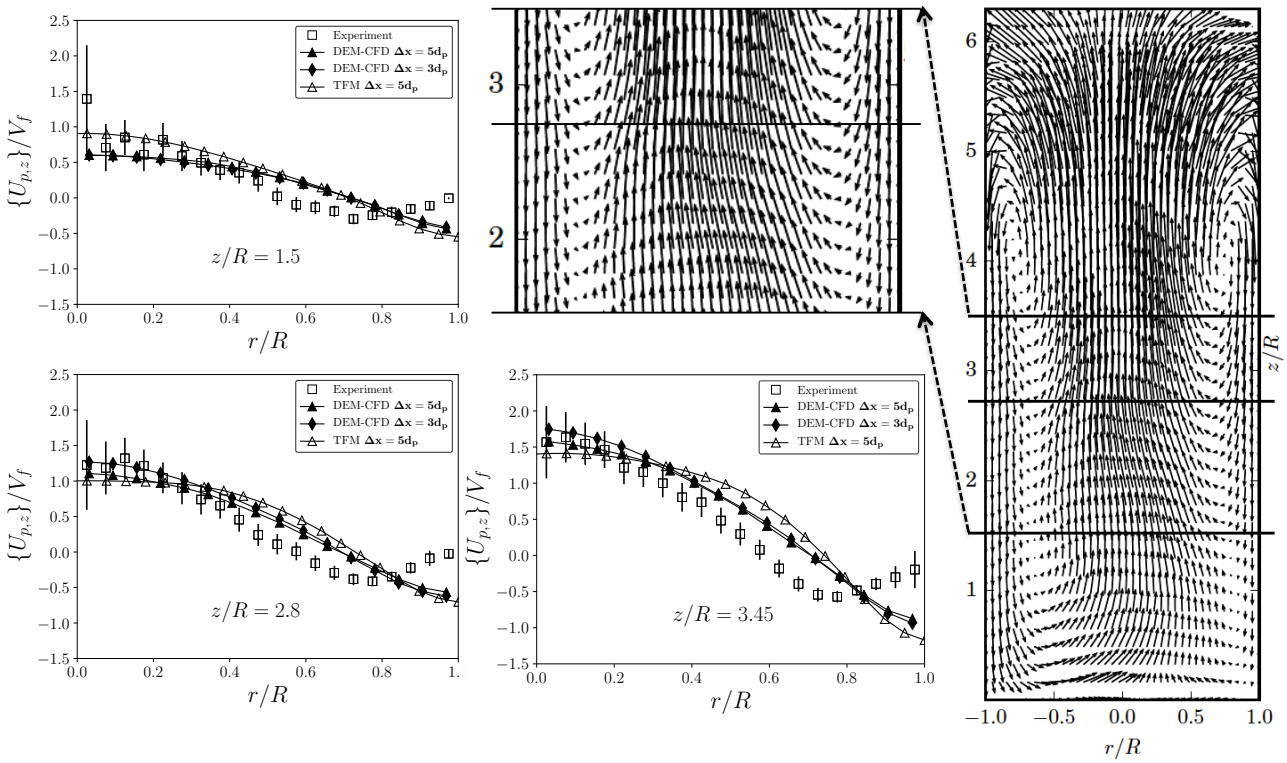

Figure 9: Radial profiles of the angle-time-averaged vertical particle velocity (RUN-I, RUN-II and the Eulerian simulation from Fede et al. (2016), corresponding to same collision parameters and free-slip boundary conditions). DEM-CFD particle velocity fields (RUN-I) on a slice in the middle of the bed.

4.3. DEM-CFD results versus experimental measurements and TFM predictions

Figure 9 compares the reference case (RUN-I) and the finest case (RUN-II) with the experimental measurements, and the TFM predictions obtained using smooth wall boundary conditions (which reduce to free slip when $\mu_w = 0$). Hereafter, figures will show TFM predictions always obtained with smooth wall boundary conditions excepted when differently mentioned. Moreover, as it was mentioned in Section 2.2, quantities predicted by a TFM approach will be compared to the measured quantities from DEM-CFD. In the case of the particle velocity, the comparison between the projected and correlated vertical particle velocity are realised. In Figure 9, the mean (angle-time-averaged) vertical particle velocity is displayed at three different locations ($z/R = 1.5, 2.8, 3.45$). According to Fede et al. (2016), the latter were chosen because the experimental error was found to be minimal at these heights. Experiments pointed out a mean upward motion of the particles in the center of the reactor and a mean downward motion in the region close to the wall, as expected. This behavior is more pronounced close to the freeboard where a large toroidal loop is located. The latter is generated by the motion of the particles coming from the bed and projecting at the bed surface with the gas. This behavior is well-known and already observed from the Eulerian simulations, in isothermal (Fede et al. (2016)) as well as in reactive conditions (Hamidouche et al. (2018)). The fluidization of the dense solid bed occurs indeed in such a way that when the superficial gas velocity becomes larger than the minimum fluidization velocity (here $V_{mf} = 0.1$ m/s), small bubbles forms in the proximity of the distributor plate. These bubbles rise into the bed and grow because of coalescence, increasing their velocity before splashing at the bed surface. This makes the bed expanding and entails the collective (mean) motion of the particles upward in the centre and downward near the wall. In the experiments, at the three heights displayed in Figure 9, the

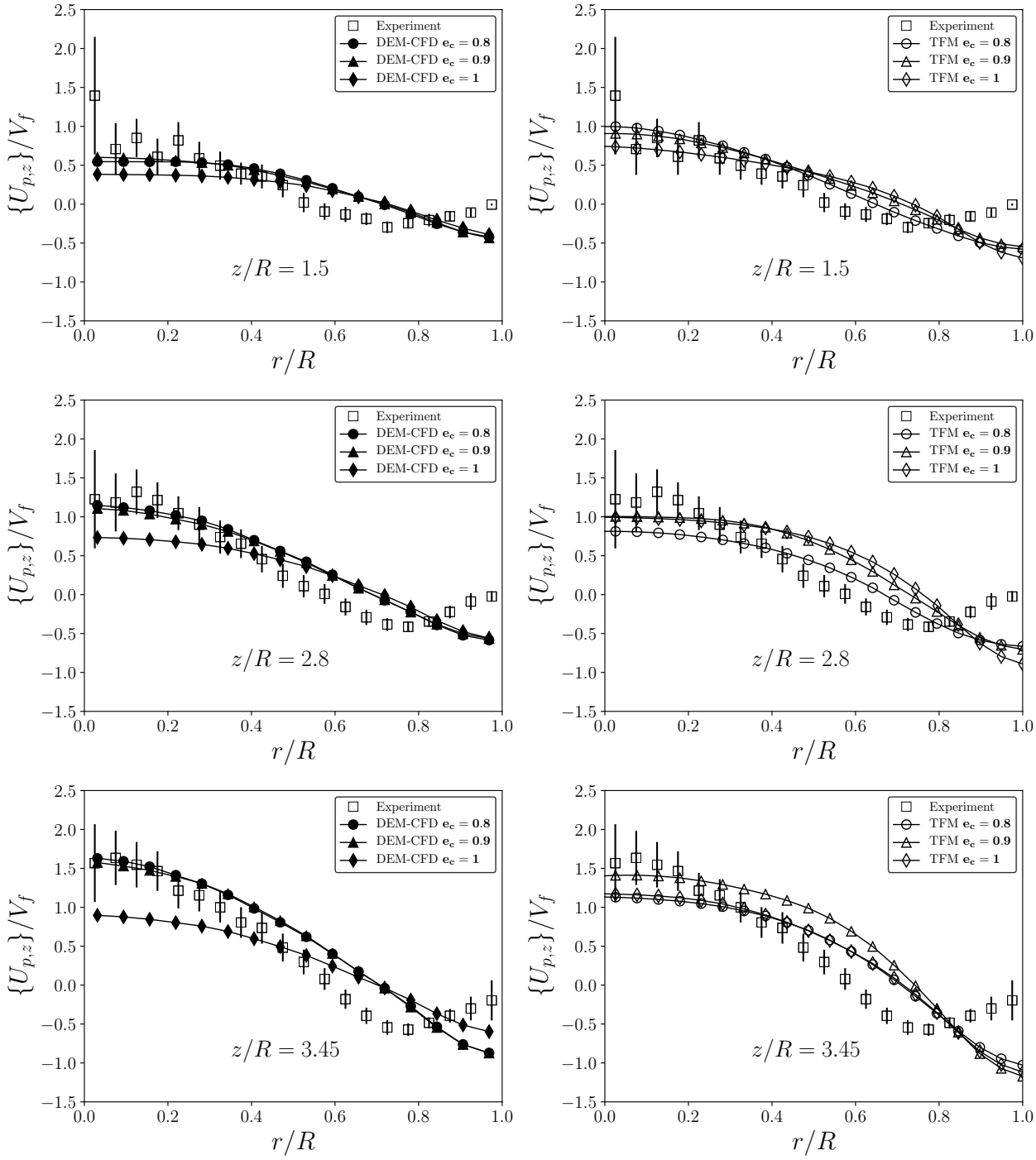

Figure 10: Radial profiles of the angle-time-averaged vertical particle velocity: effect of the particle-particle normal restitution coefficient.

highest downward velocity is observed at $r/R \simeq 0.75$, which roughly corresponds to the distance from the wall of the center of the toroidal loop. After this radial location, the slope of the profile changes and the mean particle velocity tends to zero towards the wall. Results from the DEM-CFD simulations show that in the center, both the largest and the finest mesh predict a vertical particle velocity within the error bar, similarly to the TFM approach. The two approaches differ instead from the experiments near the wall. In the work of Fede et al. (2016) this point was largely discussed. It was observed that free-slip boundary conditions were not able to predict the particle velocity near the wall, and that predictions could have been

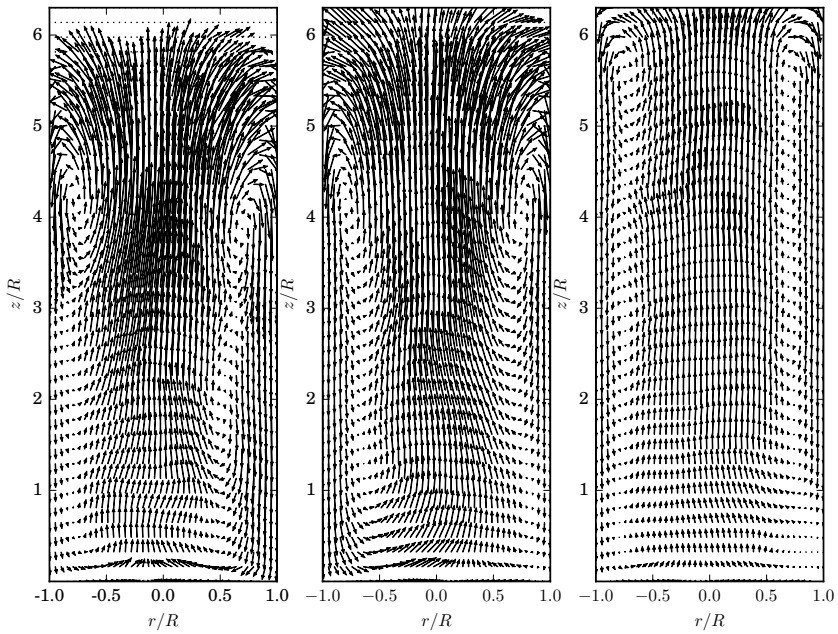

Figure 11: Effect of the particle-particle normal restitution coefficient on the time-averaged particle velocity field, on a plane in the middle of the bed. Left: $e_c = 0.8$, middle: $e_c = 0.9$, right: $e_c = 1$.

improved by using rough-wall type boundary conditions (corresponding to the no-slip conditions proposed by Fede et al. (2016) or Johnson and Jackson's (Johnson and Jackson (1987)) conditions using a large specularity coefficient ($\phi \geq 0.1$). The underlying idea was to attribute to the wall roughness the reason of such an increase of the particle-wall friction effect. This point is questioned by the present study and it will be discussed further in Section 5.

4.4. Effect of the particle-particle normal restitution coefficient

The restitution coefficient reflects the dissipation of the kinetic energy due to the inelastic deformation of the particles during the collision. In DEM-CFD simulations, numerical predictions of the mean particle velocity exhibit high sensitivity to the particle-particle restitution coefficient, as shown by Figure 10 (left panel). Data extraction at those three heights suggests that purely elastic collisions make decrease the upward particle velocity at the center of the reactor. In the frame of an Eulerian approach, a decrease of such a velocity with the increase of the restitution coefficient has already been pointed out (Dan et al. (2009)). Figure 10 shows that this effect is more remarkable in DEM-CFD than in TFM simulations (by Fede et al. (2016)). In the latter, an inverse trend is even observed at $z/R = 2.8$. There is not much difference instead between the cases corresponding to $e_c = 0.8$ and $e_c = 0.9$ in term of particle velocity predictions. It is important to note that such inelastic cases match better the experimental profiles at the reactor center than the purely elastic ones. The effect of the particle-particle normal restitution coefficient on the angle-time-averaged particle velocity field is shown by Figure 11. It is well-known that decreasing the particle-particle normal restitution coefficient makes decrease the bed height. This is due to the effect of the energy dissipation during collisions, which promotes particle clusters and large bubbles at even low fluidization velocity (Goldschmidt et al. (2001)). As a consequence, the freeboard moves towards the bottom of the reactor and the toroidal loop, signature of the particle projection at the bed surface, moves downwards as well. Differences in the mixing-loop center position are more pronounced comparing purely elastic with inelastic cases. Snapshots given the evidence of the formation of larger bubbles for lower particle-particle normal restitution coefficients are shown in Figure 12.

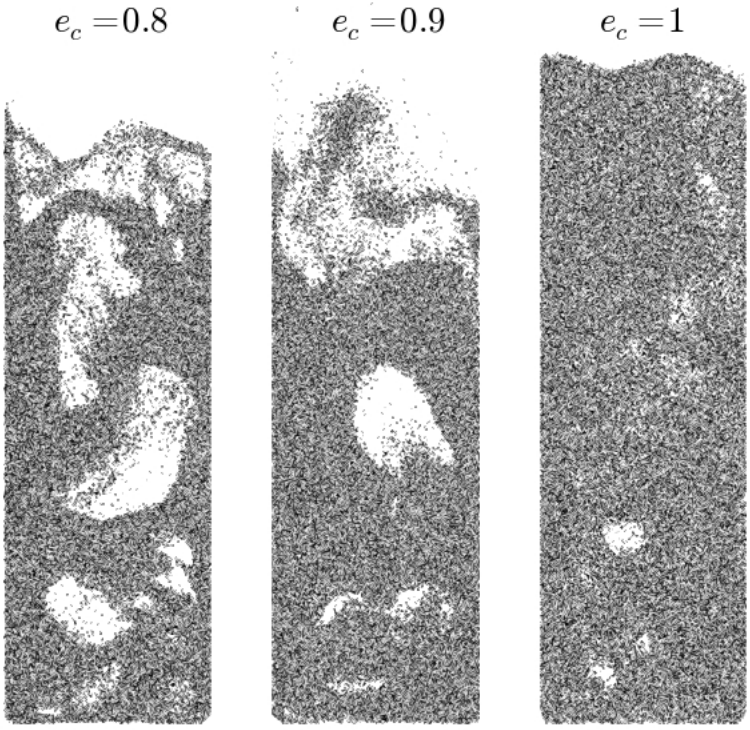

Figure 12: Snapshots of the instantaneous position of the particles within a slab taken in the middle of the bed, for different values of the normal particle-particle restitution coefficient.

4.5. Effect of the particle-wall friction

The effect of the friction at wall is here analyzed through the predictions of the mean vertical particle velocity (Figure 13). In the DEM-CFD approach, μ_w is a model parameter which explicitly characterizes the friction due to contact between each particle and the wall. In the TFM simulations (by Fede et al. (2016)), frictionless ($\mu_w = 0$) and frictional ($\mu_w > 0$) particle-wall collisions with elastic bouncing at wall ($e_w = 1$) are instead taken into account via smooth wall boundary conditions in the framework of KTGF. These boundary conditions relate the particle shear stress and the kinetic energy flux at the wall to the random kinetic energy of the particulate phase in contact with the wall and to the parameters which characterize the particle-wall collisions (Sakiz and Simonin (1999)).

First, it is observed that in the TFM simulations the particle behavior in the near wall region remains quite insensitive to the particle-wall friction, and the latter does not seem to have any substantial impact on the whole bed dynamics either. In the center of the bed, TFM predictions are also very similar regardless of the wall friction. DEM-CFD results show instead a slight decrease of the upward particle velocity at the center of the reactor when frictional conditions are accounted for. Second, as already pointed out in Section 4.4, the mean downward particle velocity is overestimated by both the approaches near the wall, in frictionless conditions ($\mu_w = 0$). The two approaches exhibit instead a very different behavior in the presence of particle-wall frictional collisions ($\mu_w = 0.3$). In particular, in DEM-CFD the effect of the friction in the near wall region is such to increase the particle velocity (with sign, i.e. to decrease the downward particle velocity) in that zone corresponding to a larger effective particle-wall friction effect, thus improving predictions compared to experimental measurements. Similar improvements were also observed by Li et al. (2012) when using a particle-wall friction coefficient $\mu_w = 0.3$ in their DEM-CFD simulations of a quasi-2D fluidized bed. The authors compared their numerical results with the experimental data of Müller et al. (2008). Noteworthy is that the same

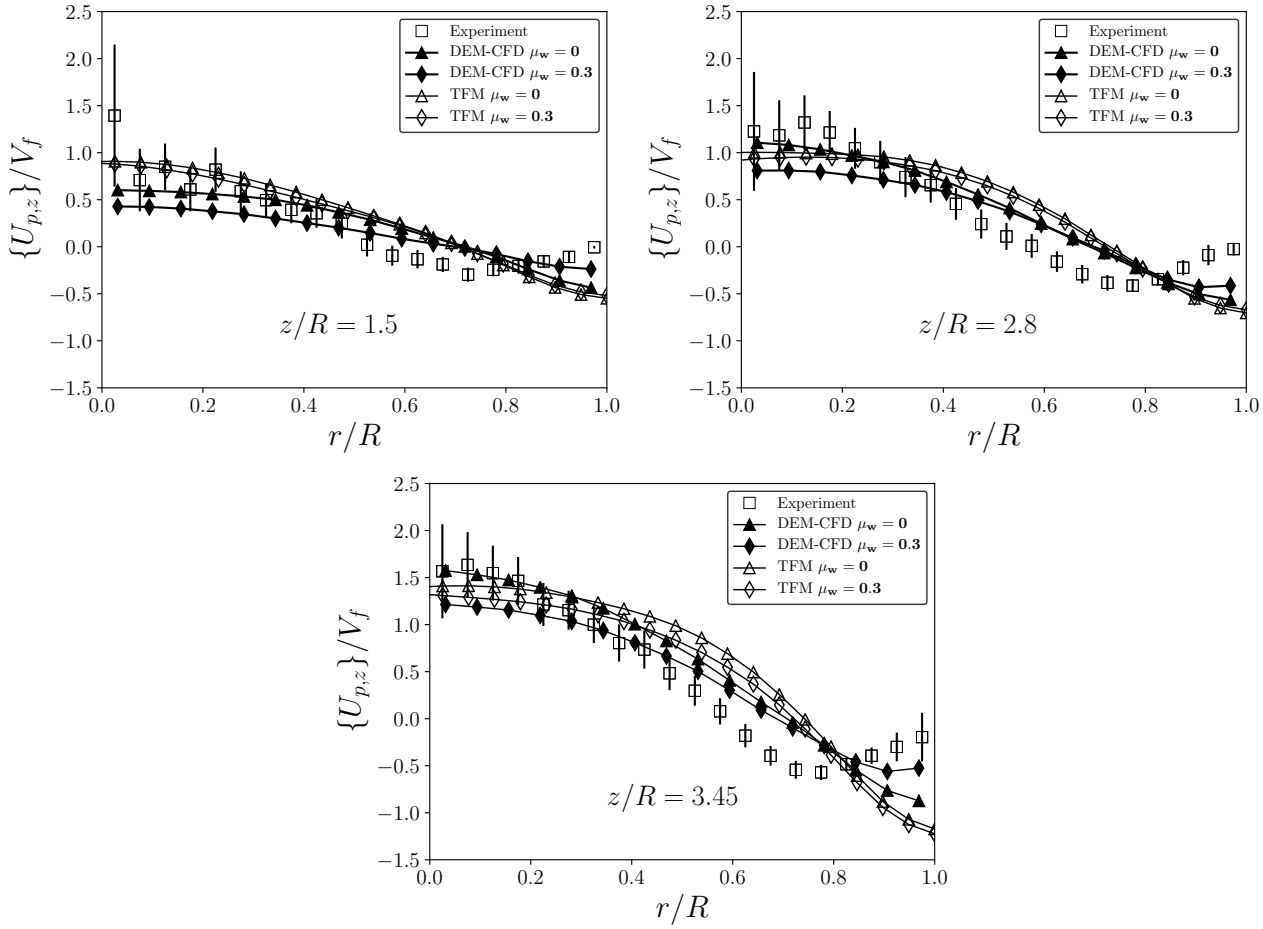

Figure 13: Radial profiles of the angle-time-averaged vertical particle velocity: effect of the particle-wall friction.

improvement may be observed with TFM if increasing the particle-wall friction effect by using no-slip conditions or rough wall boundary conditions (accounting for a stochastic component in the particle impact angle, that is Johnson and Jackson's conditions with a specularity coefficient $\phi = 0.1$) (Fede et al. (2016)). TFM results displayed in Figure 14 were obtained using no-slip boundary conditions. As shown by Figure 14, the effect of the particle-wall friction in the DEM-CFD approach is comparable to the effect of no-slip conditions in TFM. As a matter of fact, no-slip boundary conditions should represent the largest effective particle-wall friction effect accounted for by the TFM approach (zero particulate velocity near the wall). The main point raised by the present analysis is that the frictional smooth wall boundary conditions used in the frame of KTGF do not reproduce the frictional effect observed in DEM-CFD numerical simulations. The effect of the particle-wall friction on the angle-time-averaged particle velocity field is shown by Figure 15. The mixing loop corresponding to the projection of the particles at the freeboard, and signature of the large-scale behavior of the bubbling fluidized beds, is still observed in the case with particle-wall friction. However, comparison between the frictionless and frictional cases shows that the friction at the wall makes move this loop upwards. Accordingly, the bed is more expanded and a larger bed height is expected. The reason is that, because of the friction, the wall exerts on the particles a force directed upwards, which opposes the downward motion of the particles near the wall. This point will be discussed later in Section 5, when the particle-wall interactions will be investigated in detail. Furthermore, the frictional case exhibits, in average, a second loop at the bottom of the bed. Such a bottom

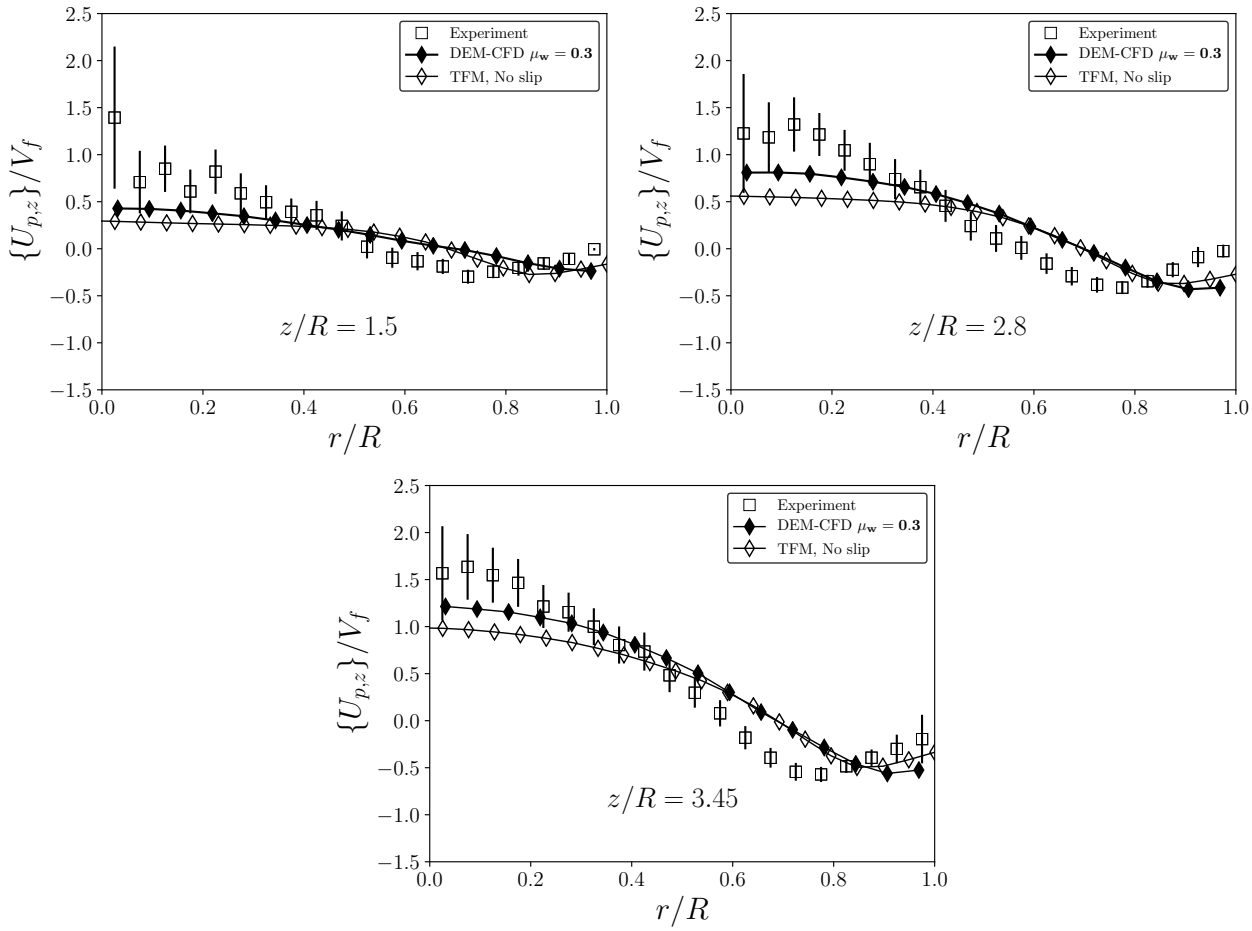

Figure 14: Radial profiles of the angle-time-averaged vertical particle velocity: comparison with no-slip boundary conditions in TFM (by Fede et al. (2016)).

loop is a counter-rotative structure compared to the upper loop. Intriguingly, two large-scale counter-rotating mixing loops were observed in the TFM simulations when no-slip or rough wall boundary conditions were used.

4.6. DEM-CFD versus TFM: further investigation.

Figure 16 shows the effect of the particle-wall friction and the particle-particle normal restitution coefficient on the vertical distribution of the time-averaged gas pressure, measured at the wall. The pressure profile is composed of two linear evolutions having different slopes (inside and outside the bed), smoothly connected at the freeboard. The upper linear profile corresponds to the hydrostatic gas pressure. The lower linear profile additionally accounts for the solid weight. A method used to roughly estimate the bed height consists of intersecting the two tangents. Accordingly, from DEM-CFD simulations an estimated bed height for the friction case is found included in the interval $4.5 \leq z/R \leq 5$ (Figure 16 (left)). For the frictionless case, the same estimate gives a slightly lower bed height ($4 \leq z/R \leq 4.5$). The two heights obtained in this way roughly match the position of the toroidal loop centers for both the frictional and frictionless test cases (Figure 15). Hamidouche et al. (2018) used the time-averaged net solid mass flux in order to evaluate the bed height. According to their results, the bed height would be slightly overestimated by the method of the tangent intersection and the loop center would be rather located above, in the freeboard. From Figure 16 (left), it is however clear that the friction at the wall acts on the particulate phase such to yield

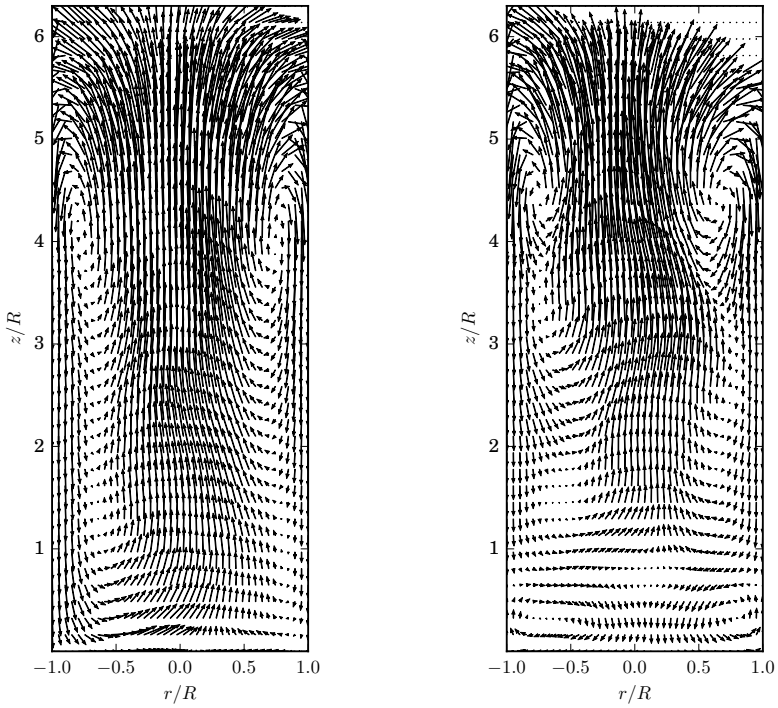

Figure 15: Effect of the particle-wall friction on the time-averaged particle velocity field, on a plane in the middle of the bed. Left: $\mu_w = 0$, right: $\mu_w = 0.3$.

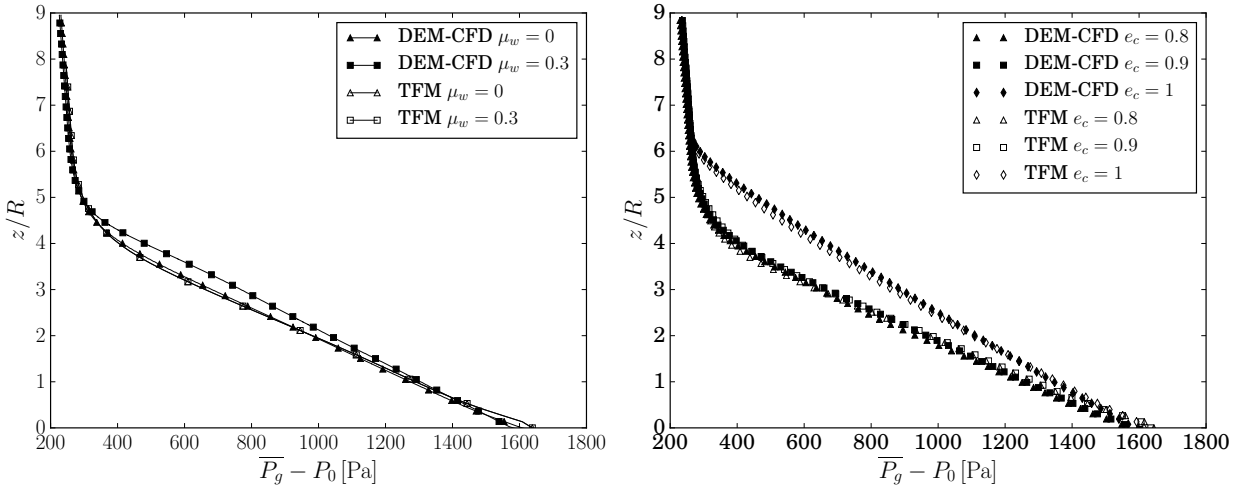

Figure 16: Vertical distribution of the time-averaged gas pressure measured at the wall. Effect of the particle-wall friction (left), effect of particle-particle normal restitution coefficient (right).

a higher bed expansion. Comparing DEM-CFD and TFM numerical predictions (Figure 16 (left)), it is observed that when $\mu_w = 0$, same mean pressure drop and bed height are obtained. Conversely, for $\mu_w = 0.3$ the TFM approach keeps unchanged the bed height so differing from the DEM-CFD results. The effect of the particle-particle normal restitution coefficient on the mean gas pressure is shown by Figure 16 (right). A substantial increase of the bed height is obtained when e_c atteins the value corresponding to purely elastic conditions, as already mentioned. Here the main information is that both DEM-CFD and TFM predict the same behavior in terms of mean pressure drop. Further information may be obtained by analyzing the mean solid fraction. Figure 17 compares DEM-CFD and TFM numerical predictions at the wall. Results show that the vertical profile of $\overline{\alpha_p}$ exhibits rather three zones. The first

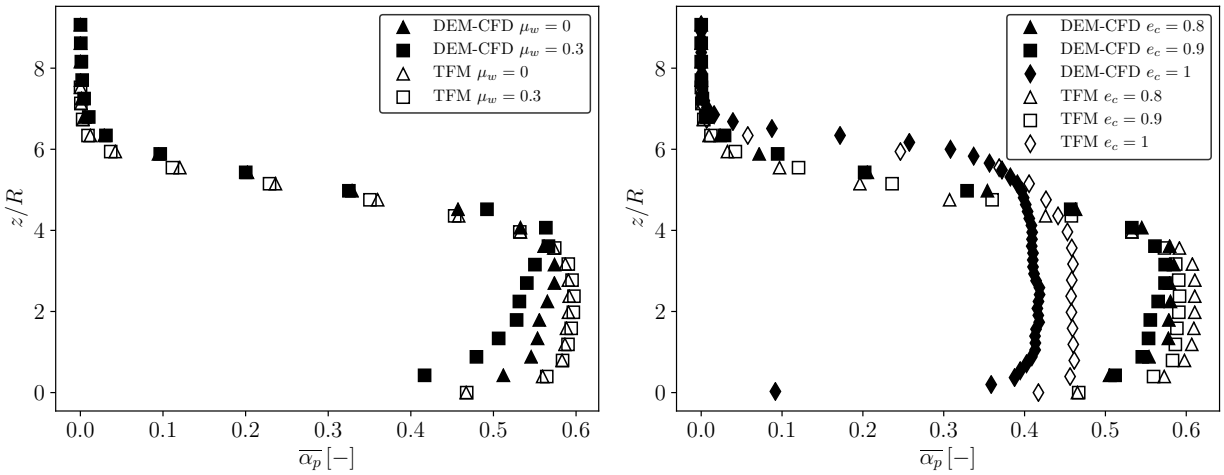

Figure 17: Vertical distribution of the time-averaged solid volume fraction measured at the wall. Effect of the particle-wall friction (left) and of the particle-particle normal restitution coefficient (right).

zone is situated at the bottom of the bed, close to the fluidization grid where small bubbles are generated. In DEM-CFD simulations, this zone differs for frictional and frictionless cases (Figure 17 (left)) because of the appearance of a counter-rotative toroidal loop in the former. Such a zone is instead identically predicted by the TFM approach using smooth wall boundary conditions, for which the two mean solid volume fraction profiles ($\mu_w = 0$ and $\mu_w = 0.3$) are almost perfectly superposed. The second zone is located into the bed (at the wall) and it exhibits a quite uniform values of $\overline{\alpha_p}$ in frictionless conditions. In this zone, in frictionless conditions, TFM slightly overestimates the mean solid volume fraction compared to the DEM-CFD simulations, but this difference is imperceptible on the mean relative pressure. Differences between the approaches are instead observed in frictional case. DEM-CFD results confirm on the mean solid volume fraction what observed on the mean relative pressure, that is, the bed height increases in the presence of friction at the wall. The same is not obtained by the TFM approach. The frictional smooth wall boundary conditions with $\mu_w = 0.3$ do not affect the vertical distribution of the solid in the reactor. In TFM simulations, this effect was observed only considering no-slip conditions or rough walls (Fede et al. (2016)). Finally, a third zone may be identified (the freeboard), where the mean solid volume fraction linearly decreases. Figure 17 (right) compares DEM-CFD and TFM numerical predictions in the case of elastic and inelastic conditions. Again, TFM seems to slightly overestimate the mean solid volume fraction compared to the DEM-CFD results. Nevertheless, globally the two approaches lead to the same behavior. Both predict a decrease of the angle-time-averaged solid volume fraction into the bed (at the wall) when e_c increases, according to the higher expansion obtained for larger particle-particle normal restitution coefficients.

The effects of the wall friction and the normal particle-particle restitution coefficient may also be observed by the radial predictions of the angle-time-averaged solid volume fraction (Figure 18). Globally, $\{\overline{\alpha_p}\}$ is lower at the center of the reactor and larger at the wall. This difference (center versus wall) is more pronounced for inelastic inter-particle collision conditions. Purely elastic particle-particle collisions lead indeed to a more homogeneous fluidized bed, as expected. The two numerical approaches slightly differ from each other quantitatively also in the radial direction, however qualitatively they exhibits same trends at all selected heights. Figure 18 (left panel) shows that in DEM-CFD the wall friction makes the solid volume fraction decrease as it promotes the bed expansion. The same is not obtained by TFM using smooth wall boundary conditions. With regard to the effect of the normal particle-particle restitution

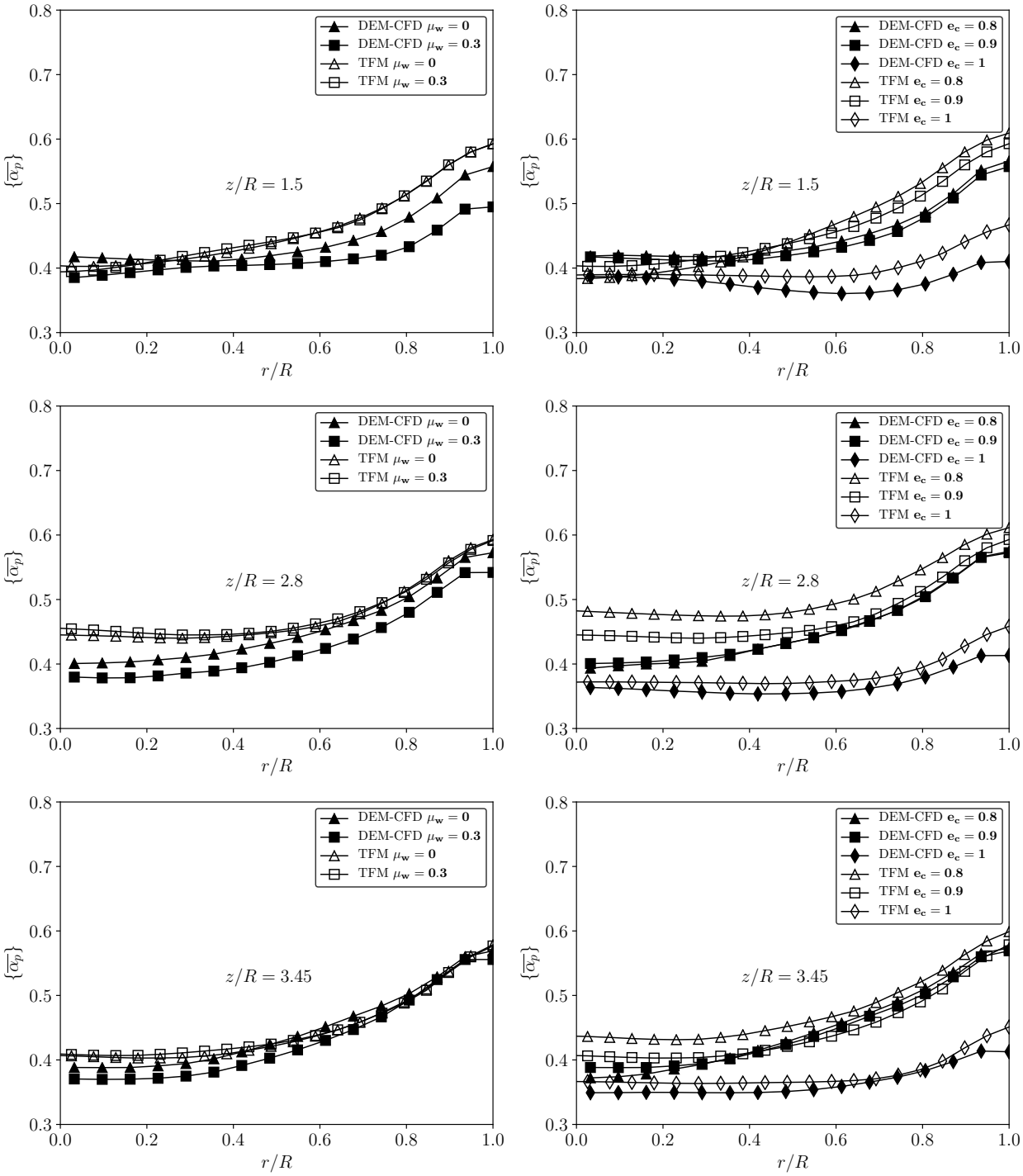

Figure 18: Radial profiles of angle-time-averaged solid volume fraction. Effect of the particle-wall friction (left) and of the particle-particle normal restitution coefficient (right).

coefficient, Figure 18 (right panel) shows that the solid volume fraction indeed increases when e_c decreases. Figure 19 shows the radial profiles of the spatial-time-averaged vertical gas velocity. The gas phase is strictly coupled with the particle motion and its velocity exhibits the same shape as the time-averaged vertical particle velocity. An upward gas velocity is observed at the center of the reactor for all the test cases. TFM yields slightly higher values than DEM-CFD in the center, at the bottom of the bed. This trend is reversed higher up in the reactor, excepted for the purely elastic case. A downward gas velocity is anticipated near the wall in

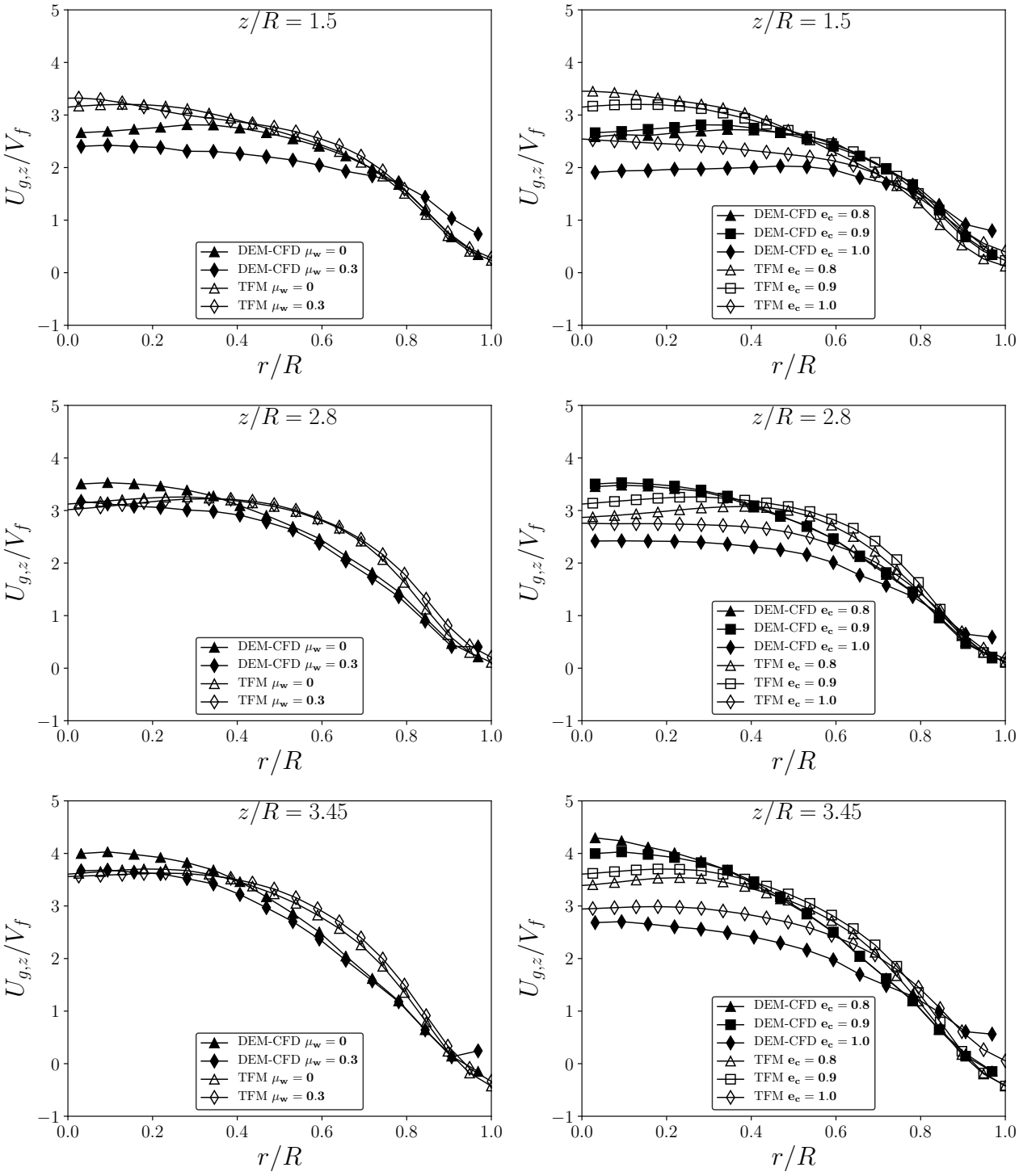

Figure 19: Radial profiles of spatial-time-averaged gas vertical velocity. Effect of the particle-wall friction (left) and of the particle-particle normal restitution coefficient (right).

the vicinity of the toroidal loop. This is expected rather above the highest selected height, as shown by Figure 20, for all the cases with the exception of the purely elastic one. Accordingly, only positives (or slightly negatives) gas velocities are depicted in Figure 19 for the DEM-CFD numerical simulations. TFM simulations exhibit higher negative gas velocities near the wall at the location $z/R = 3.45$. Differences between the two approaches near the wall are mainly observed for the frictional case and the purely elastic one. The impact of the particle-wall

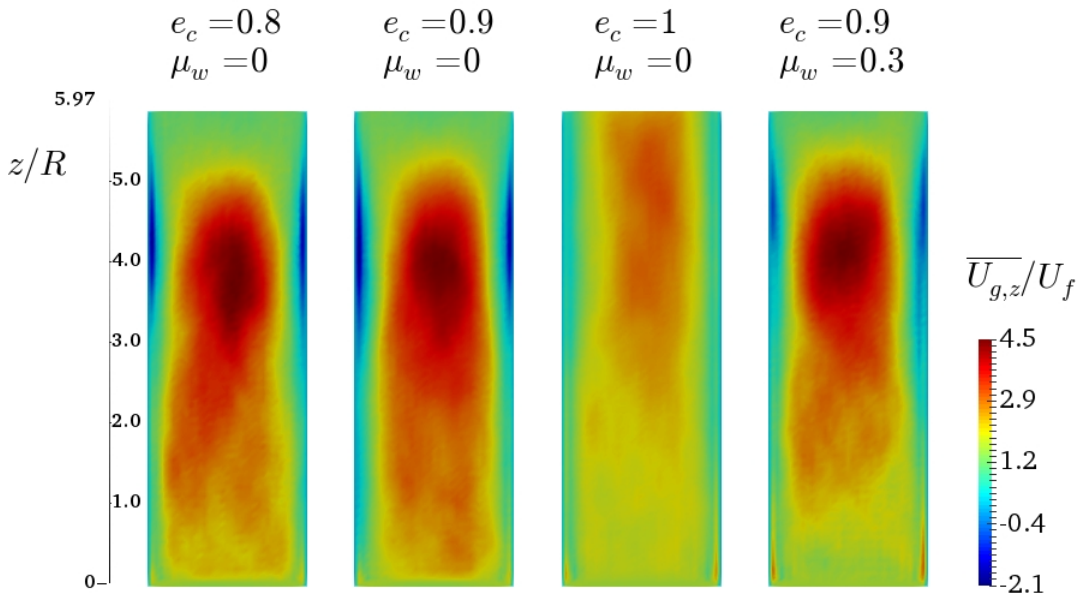

Figure 20: Time-averaged vertical gas velocity on a slice in the middle of the reactor.

friction on the gas may be examined by Figure 20, comparing the second visualization with the fourth one (from the left). The most remarkable result is that the friction at the wall makes increase the time-averaged vertical gas velocity in the near wall region, into the bed ($0 < z/R < 4$). As already mentioned (and as it will be shown in more detail in Section 5), the frictional force is upwardly directed and acts on the particulate phase such as to oppose its downward motion at the wall. As a results, the particulate velocity increases near the wall (with sign, i.e. the downward particle velocity decreases) and, because of the coupling, the gas velocity increases as well. Such an increase is stronger at the bottom of the reactor $z/R < 1$. In this zone the particles are caught in a counter-rotative motion which makes them go up near the wall and go down in the center (at large scales). Accordingly, the vertical gas velocity decreases in the center of the reactor because of the drag. In the upper part of the reactor ($z/R >\sim 4.5$) differences (with or without friction at wall) are less pronounced. As for the particles, also for the gas the effect of the particle-particle normal restitution coefficient is stronger when comparing the elastic case with inelastic cases rather than inelastic cases with each other. When $e_c = 1$, the gas velocity decreases at the center and increases at the wall in all the vertical reactor stations. The fluidized bed becomes more homogeneous and the gas velocity tends to homogenize as well.

4.7. Particle fluctuating motion characteristics

The goal of this part is mainly to compare the Eulerian particle fluctuating motion characteristics computed from the DEM-CFD results with the ones given by the TFM numerical simulations in Fede et al. (2016).

Fede et al. (2016) characterized the fluctuations of the solid volume fraction at mesoscopic scale by its variance. Its intensity is the signature of the presence of bubbles into the bed, accompanied by high local gradients of the solid volume fraction. Generally, the profiles are rather flat at the centre while they decrease sharply in the near wall region. The same trend is found by the DEM-CFD numerical simulations (Figure 21). However, DEM-CFD predicts higher intensities of the solid volume fraction variance than TFM in the center of the reactor, with the exception of the purely elastic case. For purely elastic particle-particle collisions,

DEM-CFD and TFM results superpose almost perfectly. In this case, the variance of the solid volume fraction is found much lower at the centre than in the inelastic cases. This means that α_p is locally nearly constant for the purely elastic case, corresponding to a very low bubble formation rate into the bed, as previously shown qualitatively by instantaneous visualisation (Figure 12). Globally, it is observed that the magnitude of the solid volume fraction variance increases as the normal restitution coefficient decreases, confirming the appearance of larger bubbles in the presence of inelastic particle-particle collisions. The effect of the particle-wall friction on the solid volume fraction variance is instead globally negligible, the wall friction affecting only slightly the bottom of the bed (Figure 21, left panel).

Figure 22 shows the angle-time-averaged variance of the total vertical particle velocity measured from DEM-CFD, and the time-averaged variance of the resolved vertical particle velocity as predicted by TFM, at three selected locations. Comparisons between DEM-CFD and TFM globally show a very good agreement between the two approaches for frictionless cases, even thought $\{\overline{u'_{p,z}{}^2}\}$ relies on the total particle velocity fluctuation while the TFM quantity showed in Figure 22 (referred to as $\overline{U'^2_{p,3}}$ in the original paper) represents the resolved (correlated) contribution to the total variance, in the same direction. The reason is that, as pointed out by Fede et al. (2016), the RUM kinetic energy contribution (so-called granular temperature) is very small compared to the correlated one (up to two orders of magnitude) in this direction. TFM predicts high intensities of such a mean correlated variances, meaning that the particulate flows is mainly dominated by the motion at large scales.

Figure 22 shows that in frictionless cases, values increase into the bed (below the bed surface) from the center towards the wall because of the increasing of the particle velocity gradient, then decrease in the near wall region. Increasing the particle-particle normal restitution coefficient makes the mean projected variance decrease. This is consistent with the very low bubble formation rate into the bed in the case of elastic particle-particle collisions. Bubbles indeed promote correlated fluctuations in the ascensional direction (Jung et al. (2005)). In the frictional case instead, lower intensities are predicted near the wall by the DEM-CFD simulations. In such a zone, DEM-CFD results differ substantially by TFM predictions when in the latter smooth wall boundary conditions are used. The two approaches give similar results when no-slip boundary conditions are used in TFM (see Figure 14 of Fede et al. (2016)). Accordingly, projected particle velocity fluctuations should tend to zero in the near wall regions.

Radial profiles of the diagonal components of the angle-time-averaged total particle velocity stress tensor are displayed in Figure 23, for different normal particle-particle restitution coefficients ($e_c = 0.8, 0.9, 1$) at two selected heights ($z/R = 2.8, 3.45$). The first information is that the two horizontal components $\{\overline{u'_{p,r}{}^2}\}$ and $\{\overline{u'_{p,\theta}{}^2}\}$ are close to each other at each vertical location. This implies isotropy of the fluctuation motion in horizontal planes. The second information is that the vertical component $\{\overline{u'_{p,z}{}^2}\}$ is larger than the horizontal ones, whatever the reactor height, which is the signature of a total particle velocity anisotropy in the bed. Anisotropy tends to decrease with an increase of the normal particle-particle restitution coefficient, especially in purely elastic case as observed in Figure 23.

The second contribution to the total particle kinetic energy corresponds to the RUM kinetic energy. It is given by half of the trace of the RUM stress tensor, of which an estimate is given in this work (based on the decomposition of Equation (26)) by the stress tensor defined in Equation (38). The RUM kinetic energy (usually referred to as δq_p^2, or q_p^2 in the work of Fede et al. (2016), or $\tilde{\delta} q_p^2$ in this work to indicate the estimate) is related to the granular temperature ($\Theta_p = 2/3\delta q_p^2$) most commonly defined in TFM approaches. The angle-time-averaged RUM kinetic energy, $\{\overline{\tilde{\delta} q_p^2}\}$, and the spatial-time-averaged RUM kinetic energy from

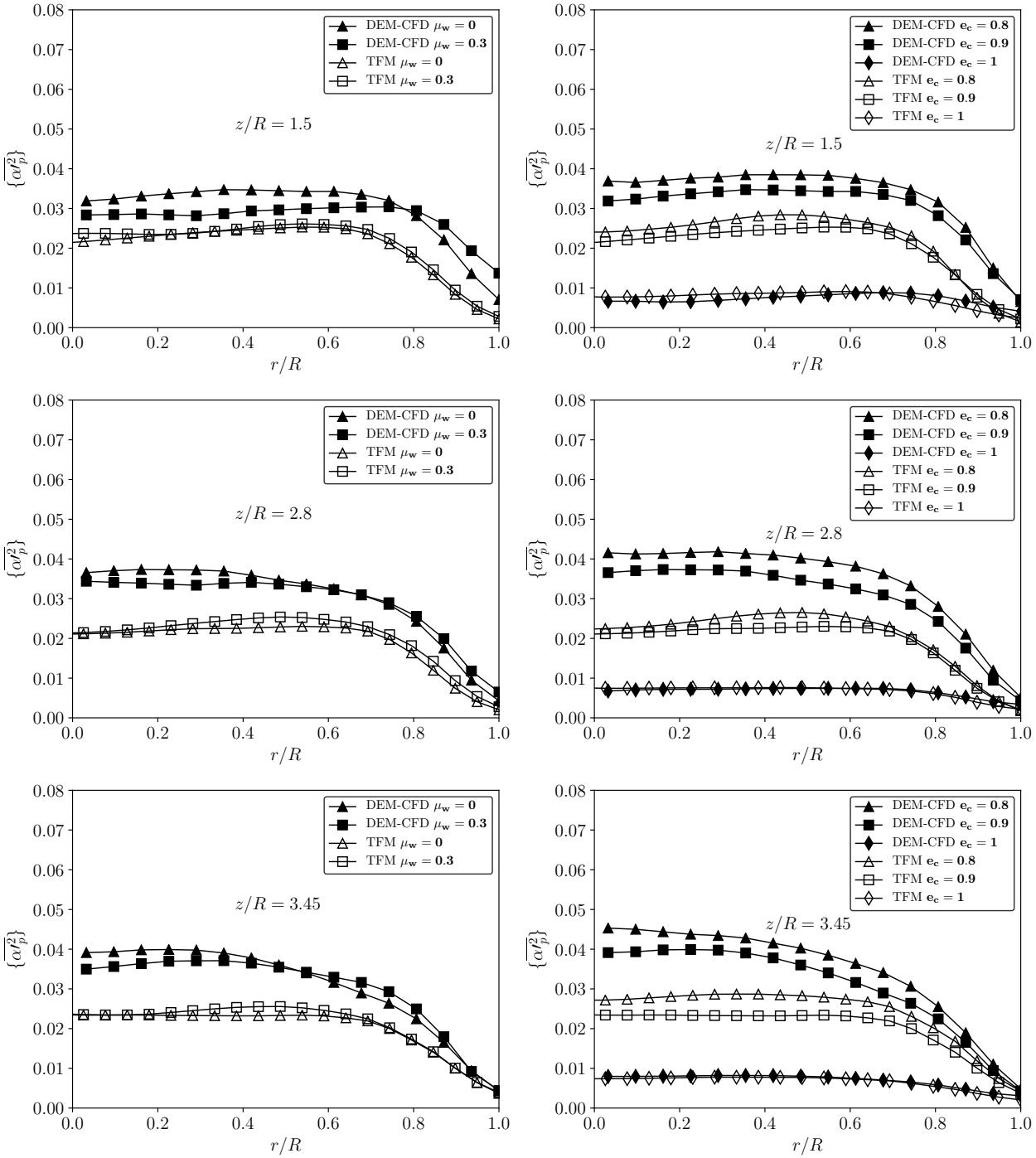

Figure 21: Radial profiles of the angle-time-averaged variance of the solid volume fraction. Effect of the particle-wall friction (left) and of the particle-particle normal restitution coefficient (right).

the TFM simulations are compared in Figure 24. For all the simulations, DEM-CFD yields larger values of such a contribution than TFM. This can be due either to a numerical insufficient accuracy in TFM numerical simulations because of the insufficient mesh refinement, or to an overestimation of $\{\overline{\tilde{\delta}q_p^2}\}$ because of the projection/interpolation procedure applied to DEM-CFD Lagrangian data (cf. Section 2.2.1). However, $\{\overline{\tilde{\delta}q_p^2}\}$ still remains very low if compared to the fluctuant total contribution (see Figure 22). Besides, DEM-CFD leads to similar conclusion as TFM concerning the very low dependency of the RUM kinetic energy from boundary effects. Similar predictions are indeed obtained with or without friction at the wall. As TFM, DEM-

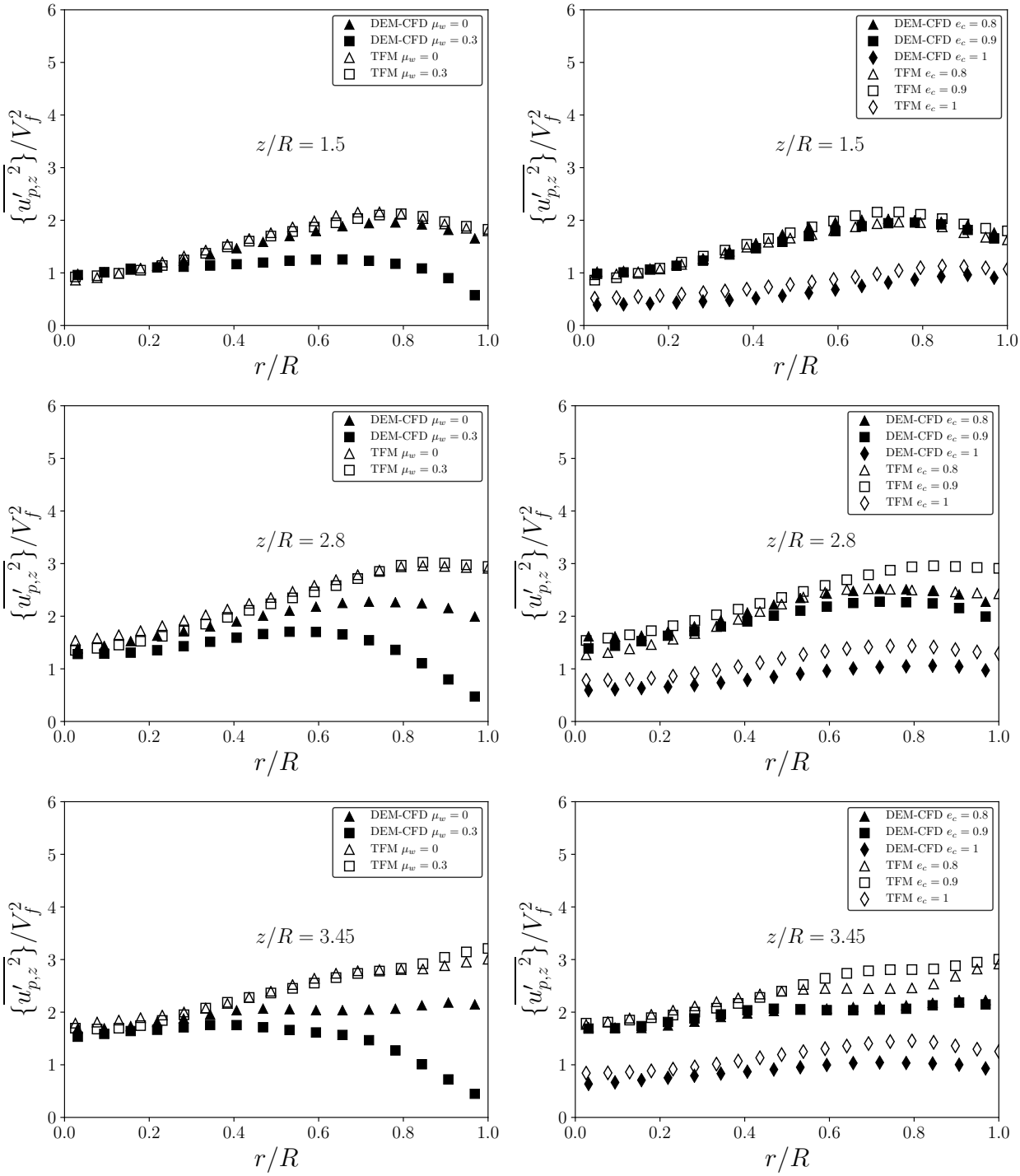

Figure 22: Radial profiles of the angle-time-averaged variance of the total vertical particle velocity. Effect of the particle-wall friction (left) and of the particle-particle normal restitution coefficient (right).

CFD predicts the largest values in purely elastic conditions. The radial profiles of the diagonal components of the angle-time-averaged RUM stress tensor are presented in Figure 25. Globally, this contribution increases with the particle-particle normal restitution coefficient because of decreasing of the energy dissipation due to inelastic collisions. Similarly to the total particle velocity stresses, also the RUM stresses exhibit anisotropy in the vertical direction, even though of smaller intensity. This anisotropy should be mainly due to the production by the correlated vertical particle velocity gradient in the radial direction.

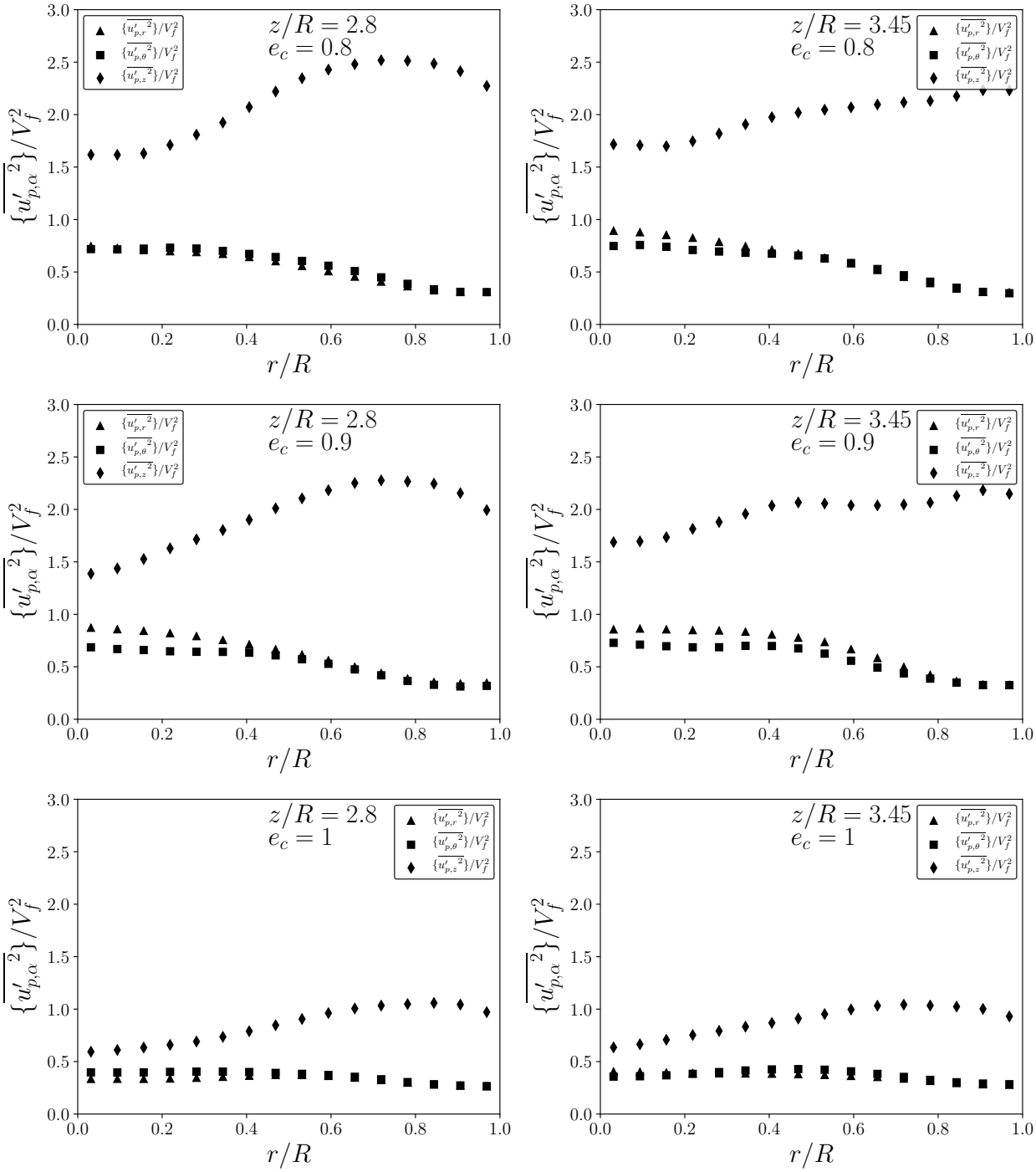

Figure 23: Radial profiles of the diagonal components of the angle-time-averaged total particle velocity stress tensor. Effect of the particle-particle normal restitution coefficient. Left: $z/R = 2.8$, right: $z/R = 3.45$.

Anisotropy in fluidized beds has been already pointed out in the literature. By experiments conducted in a quasi-2D fluidized bed configuration, Jung et al. (2005) measured the RUM particle velocity stresses (what they call laminar-type particle kinetic stresses) and correlated particle velocity stresses (referred to as Reynolds stresses), from which they deduced the particle granular temperature and the bubblelike granular temperature, respectively. Comparing vertical and lateral correlated normal stresses, they pointed out a strong anisotropy that they attributed to larger vertical particle velocity fluctuations in the bubble-flow region. Vertical normal stresses were found higher than lateral normal stresses for the RUM contribution as well,

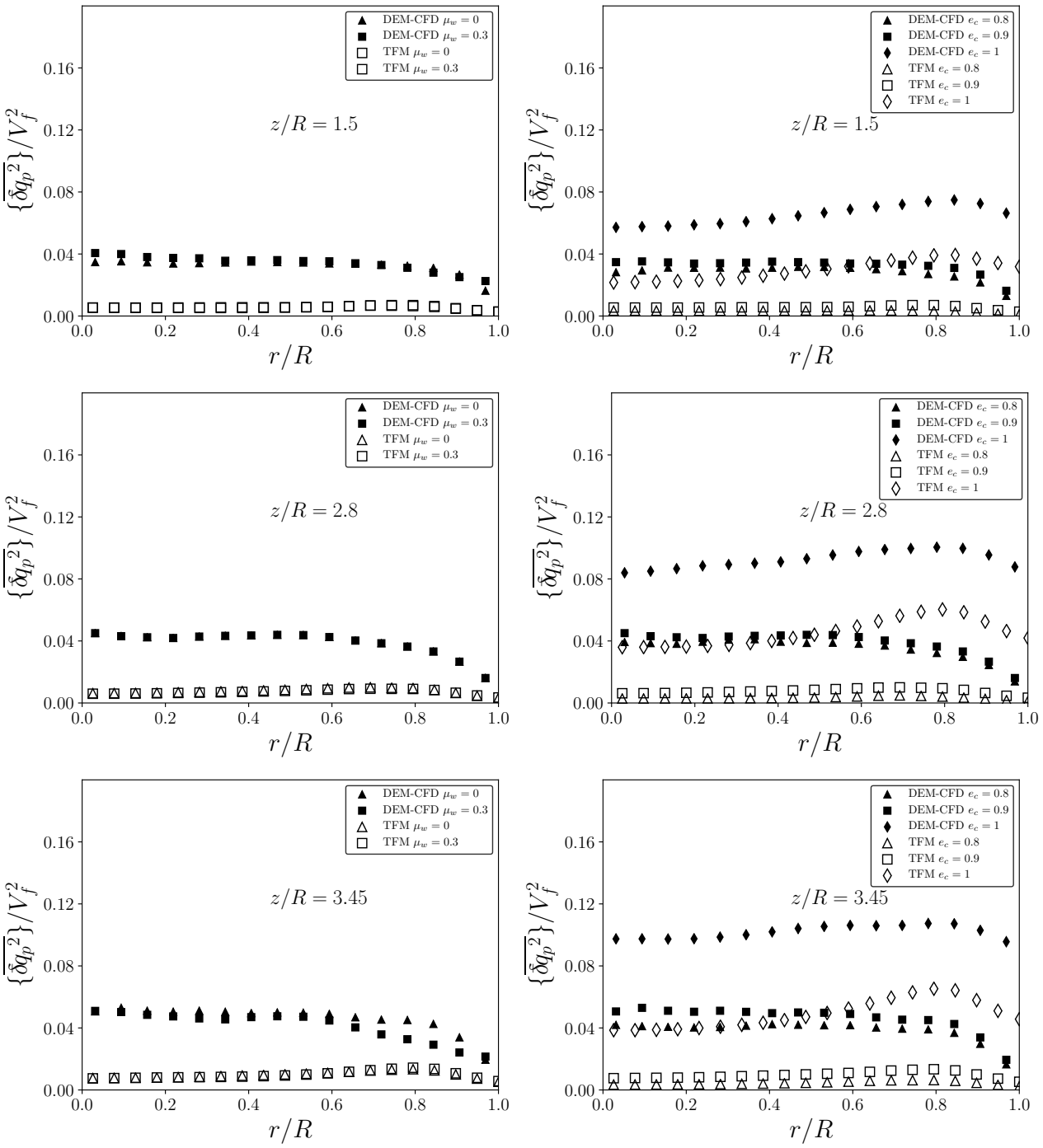

Figure 24: Radial profiles of the angle-time-averaged RUM kinetic energy. Effect of the particle-wall friction (left) and of the particle-particle normal restitution coefficient (right).

albeit less than the correlated one. Moreover, correlated stresses were found an order magnitude larger than the RUM contribution. Similar results were obtained by Müller et al. (2008), who estimated these quantities from numerical simulations performed using a DEM-CFD approach on a quasi-2D fluidized bed. Comparisons with experiments were also carried out. These authors reported a ratio between horizontal and vertical direction RUM normal stresses of ~ 0.7, on average, in their inelastic simulations. Our results for inelastic particle-particle collision are in good agreement with the results of Müller et al. (2008). They also computed bubble granular stresses and found this contribution, on average, more than an order magnitude larger then the

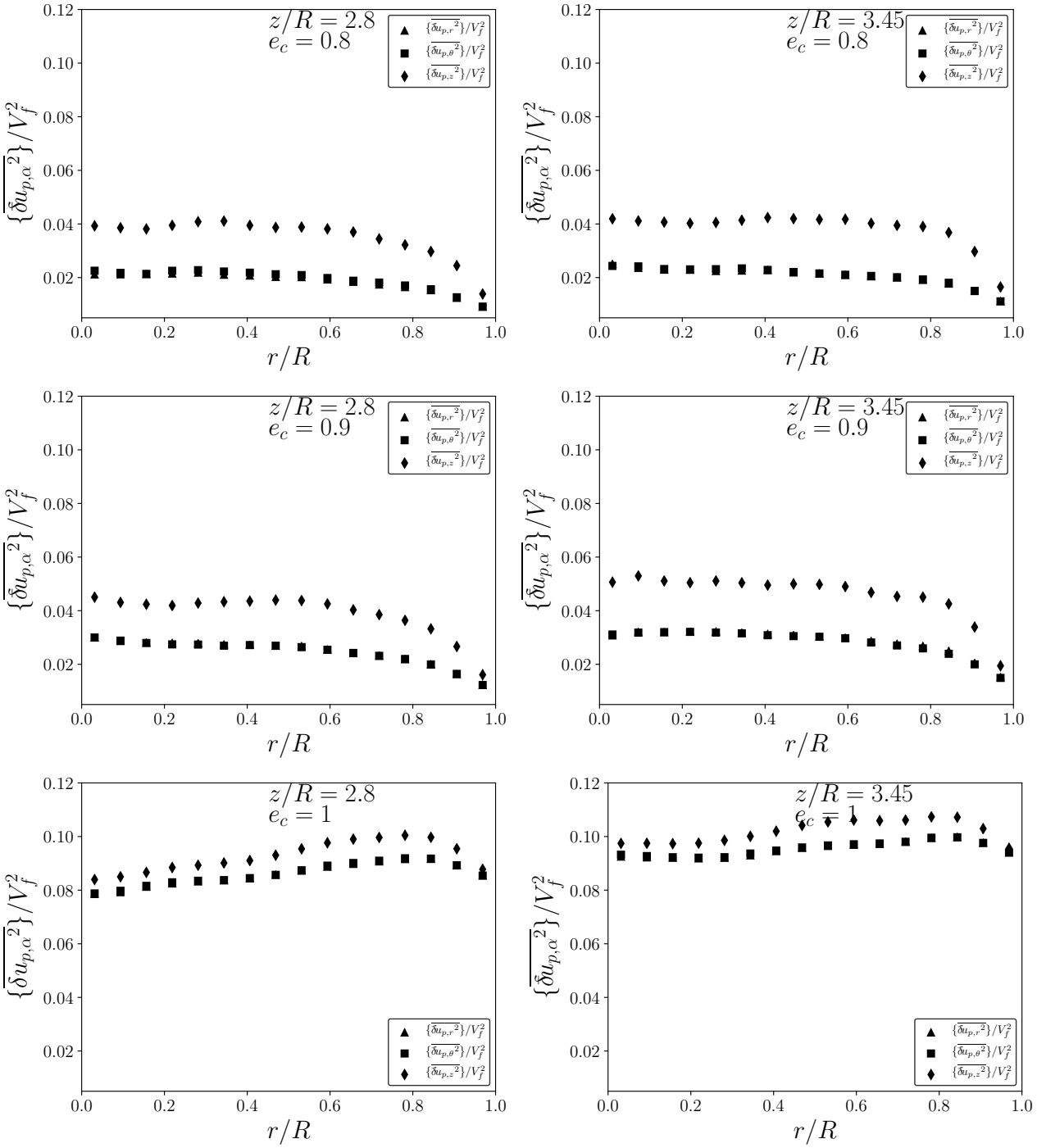

Figure 25: Radial profiles of the angle-time-averaged diagonal components of the RUM stress tensor: effect of particle-particle normal restitution coefficient. Left: $z/R = 2.8$, right: $z/R = 3.45$

RUM contribution, in vertical direction. They also observed a larger anisotropy intensity for it. Our observations confirm such results in bubbling pressurized fluidized bed as well.

5. Local analysis of particle-wall interaction

In Section 4.5 we have shown that, in the pressurized fluidized bed, the effect of friction on smooth walls predicted by the DEM-CFD approach is significantly greater than that shown by TFM simulations (of Fede et al. (2016)) for the same value of the particle-wall friction

coefficient. Therefore, to better understand the particle-wall momentum transfer effect, a local analysis is realized in the near wall region. For this purpose, the force per unit area applied by the particles on the wall is estimated from the DEM-CFD results. In perspective, this analysis seeks to improve the boundary conditions needed in the frame of the TFM approach, to apply at a distance of half a particle diameter from the wall.

The force exerted by a particle on the wall, $\mathbf{f}_{p\to w}$, or on another particle $\mathbf{f}_{q\to p}$, at a given fluid time step is computed by averaging on the collision sub-steps. Therefore, a spatial integration is performed in toroids with the same symmetry axis than the cylindrical reactor, corresponding to an arithmetic mean on the particles whose center, at a given fluid time step, is in a i-toroid with fixed widths in the radial and vertical directions:

$$(r_p(t), z_p(t), \varphi_p(t)) \in [R - \Delta r, R - d_p/2] \times [i\Delta z, (i+1)\Delta z] \times [0, 2\pi];$$

$(r_p(t), z_p(t), \varphi_p(t))$ is the particle center position in cylindrical coordinates, R is the reactor internal radius, Δr is a distance from the wall in the radial direction, and Δz is chosen equal to $10d_p$. The volume of the selected toroid is defined as $V_c = \pi((R-d_p/2)^2-(R-\Delta r)^2)\Delta z$. Different values have been chosen for the width in the radial direction, $\Delta r = 5d_p/8, 3d_p/4, dp, 3d_p/2$, in order to analyse its influence on the computation of mean quantities. Then, for any Lagrangian variable $a_p(t_{iter})$ measured at a fluid iteration for a particle whose center is in the toroid i, the overall volume and time-averaged value is defined as

$$\overline{\overline{a}}_p(z_i) = \frac{1}{\overline{\overline{N_p}}} \frac{\sum_{N_{iter}} \sum_{N_p(z_i,t_{iter})} a_p(t_{iter})}{N_{iter}}, \quad \overline{N_p(z_i)} = \frac{1}{N_{iter}} \sum_{N_{iter}} N_p(z_i, t_{iter}), \tag{42}$$

where $N_p(z_i, t_{iter})$ is the number of particles in the i-toroid at the time t_{iter}, and N_{iter} the number of fluid time steps used for time averaging.

Let us introduce $\mathbf{F}_{p\to w}(z,t) = \sum_{N_p} \mathbf{f}_{p\to w}(t)$ the total force exerted on the wall by all the particles in a given toroid, and its time averaged value

$$\overline{\mathbf{F}_{p\to w}} = \frac{\sum_{N_{iter}} \mathbf{F}_{p\to w}}{N_{iter}} = \frac{\sum_{N_{iter}} \sum_{N_p} \mathbf{f}_{p\to w}}{N_{iter}}. \tag{43}$$

Then, $\overline{\mathbf{F}_{p\to w}}/S_w$ with $S_w = 2\pi R\Delta z$ is the mean force per unit area exerted by the particles on the reactor wall.

The mean value of the vertical component of the force exerted by the particles on the reactor wall is shown in Figure 26 (left). As expected, the mean vertical force applied by the particle on the wall does not depend on the width of averaging (Δr) since the center position of all the particles interacting with the wall during a time step is situated at about a distance $d_p/2$ from the wall. Figure 26 (left) also shows that the mean vertical force applied by the assembly of particles is negative, for $z/R \geq 1$, and becomes positive below. As also expected, the mean vertical force, which corresponds to the mean friction exerted by the particle assembly on the wall, is always in the same direction than the mean vertical velocity in the very near wall region (see Figure 26 (right)). In addition, the maximum of the mean force applied by the particles on the wall is measured at $z/R \simeq 4.2$ while the maximum of the mean particle vertical velocity is found at $z/R \simeq 5.5$. But the particle-to-wall friction effect is also depending on the solid volume fraction and on the particle velocity variance (see Section 4.6 and Section 4.7).

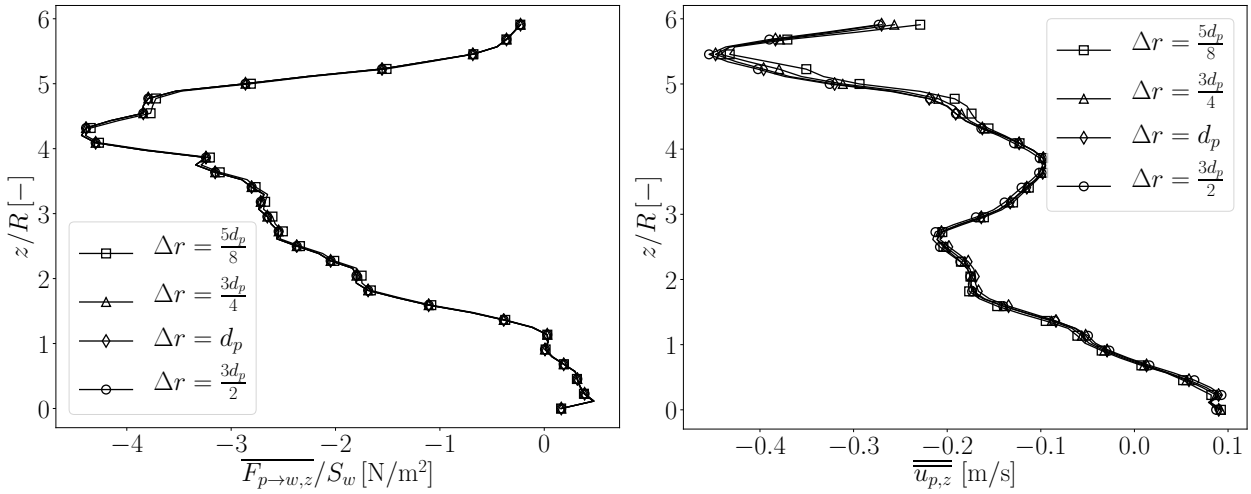

Figure 26: Vertical distribution of the mean vertical force per unit area exerted on the boundary by the particles (left) and of the mean vertical particle velocity in the near wall region (right) measured for the particles whose center is situated at a distance less than $\Delta r = 5d_p/8, 3d_p/4, d_p, 3d_p/2$ from the wall.

According to Johnson and Jackson (1987), the force per unit area on the boundary may be written in the frame of KTGF as the sum of collisional and frictional stress contributions. The first contribution corresponds to the effect of short contacts occurring when particles are widely spaced and are bouncing on the wall, while the second contribution corresponds to the effect of particle to wall contacts sustaining for long times which may occur when particles are very close to each other. Therefore, following Johnson and Jackson (1987), the instantaneous tangential force on a small surface element δS_w applied by particle assembly on the wall can be written as follows:

$$\delta \mathbf{F}_{p\to w} \cdot \widetilde{\boldsymbol{\tau}}_p = \Sigma_w^{coll} \delta S_w + \Sigma_w^{fr} \delta S_w. \tag{44}$$

$\widetilde{\boldsymbol{\tau}}_p$ represents the tangential vector to the wall aligned with the correlated velocity of the particle assembly, $\widetilde{\mathbf{u}}_p$, measured at a distance $d_p/2$,

$$\widetilde{\boldsymbol{\tau}}_p = \frac{\widetilde{\mathbf{u}}_p - (\widetilde{\mathbf{u}}_p \cdot \mathbf{n})\mathbf{n}}{|\widetilde{\mathbf{u}}_p - (\widetilde{\mathbf{u}}_p \cdot \mathbf{n})\mathbf{n}|}, \tag{45}$$

with $\mathbf{n}$ the unit vector normal to the wall and directed towards the flow. In Equation (44), Σ_w^{coll} represents the tangential momentum transferred per the frictional collisions of short duration and, in the case of Coulomb's law with full sliding collision on smooth surface, it may be written (Sakiz and Simonin (1999)) as

$$\Sigma_w^{coll} = n_p m_p \mu_w^{coll} \langle \delta u_{p,n} \delta u_{p,n} \rangle, \tag{46}$$

where the operator $\langle \cdot \rangle$ represents an ensemble average defined in the frame of the statistical probability density function (PDF) approach, $\delta u_{p,n}$ is the RUM particle velocity fluctuation in the wall-normal direction, and μ_w^{col} is the Coulomb friction coefficient for sliding collision. Σ_w^{fr} represents the shear component of the frictional stress applied by the particles to the wall and for Coulomb's friction model may be written as $\Sigma_w^{fr} = \mu_w^{fr} P_w^{fr}$ where P_w^{fr} represents the normal component of the particulate frictional stress applied to the wall and μ_w^{fr} is the friction coefficient of Coulomb's law applied to the particle sliding for long times over the wall surface. In the frame of the soft-sphere DEM-CFD approach used in this work, the following equalities are imposed

$$\mu_w^{fr} = \mu_w^{coll} = \mu_w. \tag{47}$$

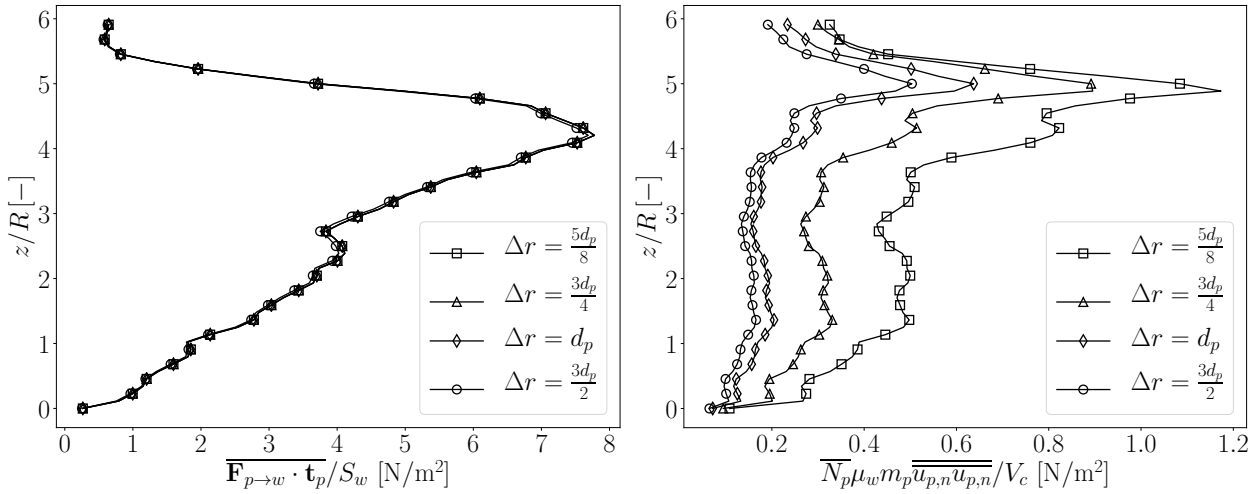

Figure 27: Vertical distribution of the mean tangential force per unit area exerted on the boundary by the particles (left) and of the mean collisional term at the wall (right), computed from the wall-normal velocity of particles whose center is situated at a distance less than $\Delta r = 5d_p/8, 3d_p/4, d_p, 3d_p/2$ from the wall.

To evaluate the decomposition of the particle momentum transferred to the wall, an integration of Equation (44) on the surface of the toroid averaging over time can be carried out

$$\frac{\overline{\mathbf{F}_{p\to w}\cdot\widetilde{\boldsymbol{\tau}}_p}}{S_w} = \overline{\Sigma_w^{coll}} + \overline{\Sigma_w^{fr}}, \tag{48}$$

where the mean collisional term is computed as

$$\overline{\Sigma_w^{coll}} = \overline{N_p} m_p \mu_w \frac{\overline{\overline{u_{p,n}u_{p,n}}}}{V_c}. \tag{49}$$

In practice, the unit vector $\widetilde{\boldsymbol{\tau}}_p$ aligned on the particle assembly tangential velocity is approximated by the unit vector $\mathbf{t}_p$ aligned with the discrete particle tangential velocity given by

$$\mathbf{t}_p = \frac{\mathbf{u_p} - (\mathbf{u_p}\cdot\mathbf{n})\mathbf{n}}{|\mathbf{u_p} - (\mathbf{u_p}\cdot\mathbf{n})\mathbf{n}|}. \tag{50}$$

In Equation (49) the RUM velocity fluctuation $\delta u_{p,n}$ was assumed to be equal to the instantaneous wall-normal particle velocity $u_{p,n}$ and replaced by it. In fact, without deposition, the projected radial velocity at the distance $d_p/2$ from the wall should be equal to zero. Indeed, for particles whose center is at a distance less than $3d_p/4$ from the wall we found $\overline{\overline{u_{p,n}}} < 10^{-4}\sqrt{\overline{\overline{u_{p,n}u_{p,n}}}}$. Accordingly, Equation (48) is rewritten as follows:

$$\frac{\overline{\mathbf{F}_{p\to w}\cdot\mathbf{t}_p}}{S_w} = \overline{N_p} m_p \mu_w \frac{\overline{\overline{u_{p,n}u_{p,n}}}}{V_c} + \overline{\Sigma_w^{fr}}. \tag{51}$$

The vertical distribution of the mean tangential force per unit area transferred to the boundary by the particles, $\overline{\mathbf{F}_{p\to w}\cdot\mathbf{t}_p}/S_w$, and the vertical distribution of the collisional term, $\overline{N_p} m_p \mu_w \frac{\overline{\overline{u_{p,n}u_{p,n}}}}{V_c}$, are displayed in Figure 27. The latter clearly shows that the mean force exerted on the boundary by the particles is significantly greater than the collisional contribution, and that, according to Equation (51), the dominant contribution is the particle-wall frictional stress contribution

$$\frac{\overline{\mathbf{F}_{p\to w}\cdot\mathbf{t}_p}}{S_w} \approx \overline{\Sigma_w^{fr}}. \tag{52}$$

The frictional stress contribution due to the long contact duration was neglected in the TFM simulations by Fede et al. (2016)) using frictional smooth wall boundary conditions; this should justify the large underestimation of the particle friction at the wall compared to the DEM-CFD predictions, as shown in Section 4.5. Figure 27 (left) shows the vertical profile of $\overline{\mathbf{F}_{p\to w}\cdot\mathbf{t}_p}/S_w$. The latter is always positive and takes a maximum at $z/R\simeq 4.2$ as the quantity $|\overline{F_{p\to w,z}}/S_w|$ (see Figure 26 (left)). Moreover, the measured values of $\overline{\mathbf{F}_{p\to w}\cdot\mathbf{t}_p}/S_w$ are found about twice those of $|\overline{F_{p\to w,z}}/S_w|$. From these results we can deduced that the force projected on the particle velocity direction, $\overline{\mathbf{F}_{p\to w}\cdot\mathbf{t}_p}$, is the mean of the absolute value of the instantaneous friction of the particles on the wall. In contrast, in the formulation of $\overline{F_{p\to w,z}}/S_w$ the instantaneous friction contribution in the given vertical direction may be positive or negative according to whether particles move up or down, leading to the lower computed mean value.

According to Johnson and Jackson (1987), the vertical momentum balance written on an elementary cell with a wall-normal width tending towards zero leads to an equilibrium between the momentum transferred from the flow to the near wall region and that transferred from the wall. Such an equilibrium can be written as

$$\delta F_{q\to p,z} - n_p m_p \langle u_{p,n} u_{p,z}\rangle \delta S_w + \delta F_{w\to p,z} = 0, \tag{53}$$

where the first term on the left-hand side represents the force exerted by the outside q-particles on the p-particles with center in the elementary cell, while the second term represents the wall-normal transport of the vertical momentum by the instantaneous particle velocity. In the very near wall region, $\widetilde{u}_{p,n}\to 0$ and the velocity correlation is reduced to the RUM kinetic shear stress $\langle \delta u_{p,n}\delta u_{p,z}\rangle$ which represents the transport by the wall-normal RUM velocity (Sakiz and Simonin (1999)). The third term on the left hand-side represents the force exerted by the wall on the particle with center in the elementary cell, $\delta\mathbf{F}_{w\to p}=-\delta\mathbf{F}_{p\to w}$. Then, Equation (53) may be integrated on the toroid wall surface and time-averaged, so to write

$$\frac{\overline{F_{q\to p,z}}}{S_w} - \overline{N_p} m_p \frac{\overline{\overline{u_{p,n}u_{p,z}}}}{V_c} = -\frac{\overline{F_{w\to p,z}}}{S_w} = \frac{\overline{F_{p\to w,z}}}{S_w}. \tag{54}$$

Equation (54) represents an equality between the mean flux of the vertical momentum incoming across the surface positioned at $R-\Delta r$ (collisional, frictional, kinetic) and the flux incoming across the surface at $R-d_p/2$ due to the interaction with the wall (collisional, frictional). On the left-hand side of Equation (54), $\overline{F_{q\to p,z}}$ is the mean vertical particle-particle collision force measured in the near wall region and the second term, $\overline{N_p} m_p \overline{\overline{u_{p,n}u_{p,z}}}/V_c$, represents the mean transport of vertical momentum by the RUM wall-normal velocity fluctuation.

Figure 28 (right) shows the vertical profile of $\overline{N_p} m_p \overline{\overline{u_{p,n}u_z}}/V_c$, computed from velocities of particles whose center is situated at a distance less than $\Delta r = 5d_p/8, 3d_p/4, d_p, 3d_p/2$ from the wall. It can be seen that the term $\overline{N_p} m_p \overline{\overline{u_{p,n}u_{p,z}}}/V_c$ is negligible compared to the other terms in Equation (54). Therefore, as expected, the mean vertical forces per unit area $\overline{F_{p\to w,z}}/S_w$ (Figure 26 (left)) and $\overline{F_{q\to p,z}}/S_w$ (Figure 28 (left)) are nearly equal.

These results show that, for the DEM-CFD case (RUN-V) investigated here, the mean transfer of the particle vertical momentum from the flow to the near-wall region by the kinetic shear stress is negligible compared to the transfer by direct inter-particle interactions. In the KTGF approach, this means that the inter-particle collisional and frictional shear stress contributions are dominant over the kinetic shear stress contribution, as expected in dense regime. Moreover, for the DEM-CFD case investigated here, the inter-particle collisions are assumed inelastic and frictionless leading to zero contribution of the inter-particle frictional shear stress, in agreement with the model assumption of the TFM simulations by Fede et al. (2016). Therefore, such an approach should be able to represent the same behavior than the

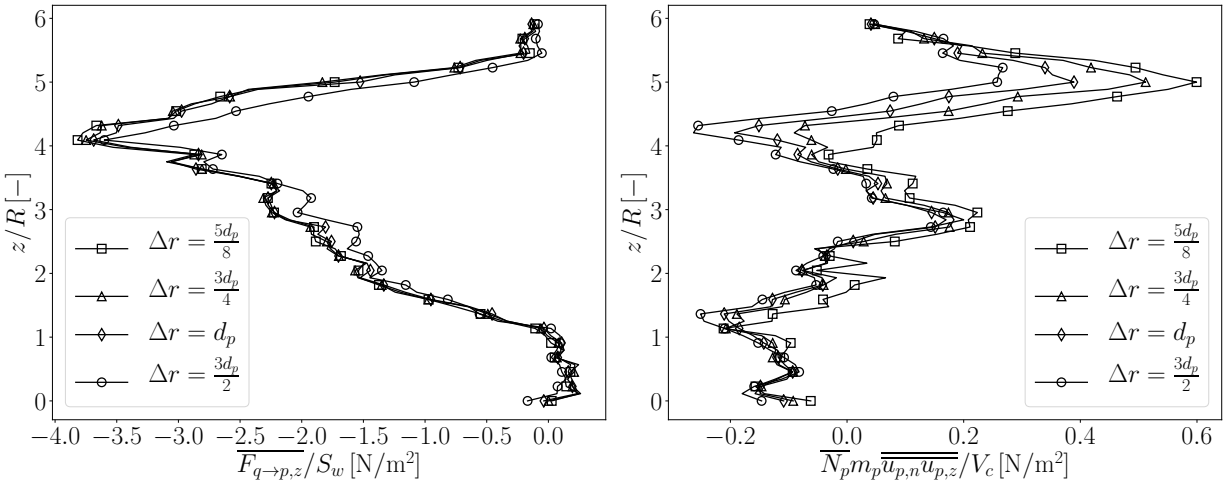

Figure 28: Vertical distribution of the mean vertical particle-particle collision force per unit area (left) and of the mean kinetic term in the near wall region (right), computed from particles whose center is situated at a distance less than $\Delta r = 5d_p/8, 3d_p/4, d_p, 3d_p/2$ from the wall.

DEM-CFD simulation for the transfer of the vertical particle momentum from the flow to the wall if the particle velocity boundary conditions are supplemented by the frictional effect.

Finally, according to Johnson and Jackson (1987) we may assume that, during the DEM-CFD simulations of the lab-scale dense pressurized bed, the mean frictional effect is due, on the one hand, to the effect of the short particle-wall contacts in dilute regime and, on the other hand, to the long sustained contacts of the particle clusters in dense regime. In the frame of the KTGF approach, in dilute regime, the inter-particle collisional and frictional shear stress contributions at the wall and the particle-wall frictional stress contribution are negligible and the following equality (Sakiz and Simonin (1999)) should be verified

$$n_p m_p \langle \delta u_{p,n} \delta u_{p,\tau} \rangle = -n_p m_p \mu_w \langle \delta u_{p,n} \delta u_{p,n} \rangle, \tag{55}$$

where $\delta u_{p,\tau}$ is the RUM velocity fluctuation projected on the wall, $\delta u_{p,\tau} = \delta \mathbf{u}_p \cdot \widetilde{\boldsymbol{\tau}}_p$. This equality is equivalent to Equation (53), but written along the direction of the projected particle velocity projection on the wall $\widetilde{\boldsymbol{\tau}}_p$.

On the other hand, in dense regime, when the particles are very close to each other, they slide together along the wall and we may assume that the wall-normal discrete particle velocity is nearly equal to zero leading to a zero value for the wall-normal particle RUM velocity correlations. Therefore, we should have the equality

$$n_p m_p \langle \delta u_{p,n} \delta u_{p,\tau} \rangle = -n_p m_p \mu_w \langle \delta u_{p,n} \delta u_{p,n} \rangle = 0. \tag{56}$$

It follows that whatever the regime, dilute or dense, such an equality is verified. Figure 29 shows the volume and time average of the correlation between the tangential and the wall-normal velocity, $N_p m_p \overline{\overline{u_{p,n} u_{p,t}}}/V_c$. Comparison with Figure 27 (right) shows that, in agreement with the above analysis,

$$\overline{N_p} m_p \overline{\overline{u_{p,n} u_{p,t}}}/V_c \approx -\overline{N_p} m_p \mu_w \overline{\overline{u_{p,n} u_{p,n}}}/V_c \tag{57}$$

when $\Delta r - d_p/2 \to 0$.

To conclude, these late results are consistent with the Johnson and Jackson (1987) proposition leading to write the wall-tangential particle velocity boundary condition as

$$\delta \mathbf{F}_{q\to p} \cdot \widetilde{\boldsymbol{\tau}_p} - n_p m_p \langle \delta u_{p,n} \delta u_{p,\tau} \rangle \delta S_w = \Sigma_w^{coll} \delta S_w + \mu_w^{fr} P_w^{fr} \delta S_w. \tag{58}$$

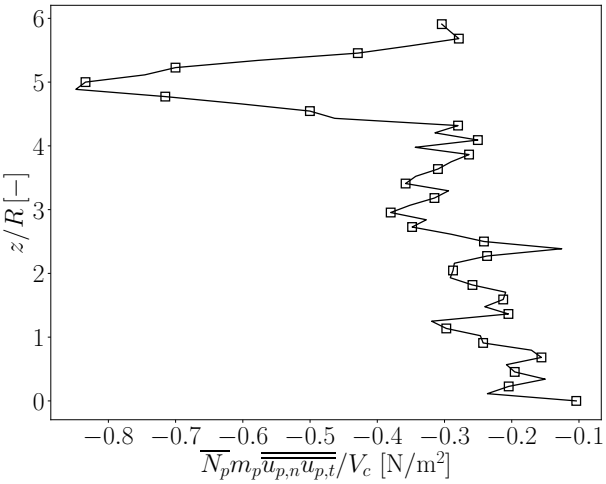

Figure 29: Vertical distribution of the mean correlation between the wall-normal and tangential particle velocity components in the near wall region, computed from particles whose center is situated at a distance less than $\Delta r = 5d_p/8$ from the wall.

Therefore, in the frame of the viscosity assumption for the particulate stress and Coulomb's frictional sliding on smooth wall (Sakiz and Simonin (1999)), the wall boundary condition on the projected particle velocity wall-tangential component should be written as

$$n_p m_p \nu_p \frac{\partial \widetilde{u}_{p,\tau}}{\partial n} = n_p m_p \mu_w^{coll} \Theta_p + \mu_w^{fr} P_w^{fr}, \tag{59}$$

where ν_p represents the particulate phase effective kinematic viscosity, modeling the kinetic, collisional and frictional particulate shear stresses. Θ_p is the granular temperature and P_w^{fr} represents the normal component of the particulate frictional stress applied to the wall. μ_w^{coll} and μ_w^{fr} represent the Coulomb's dynamic friction coefficients for short time collisions and sustained contacts, respectively.

6. Conclusion

In this work, numerical simulations of a lab-scale pressurized dense fluidized bed were performed in the frame of a soft-sphere DEM-CFD approach. Such an approach provided a detailed description of the particle-particle and particle-wall interactions allowing to investigate the effect of the normal particle-particle restitution coefficient and of the particle-wall friction on the overall dense particle bed behavior. Comparisons between numerical DEM-CFD results and experimental measurements (Fede et al. (2009)) were carried out on the time-averaged vertical particle velocity. A very good agreement was obtained at the center of the reactor, while an overestimation of the downward vertical particle velocity was observed in the near wall region. Accounting for the particle-wall friction effects in the DEM-CFD numerical simulations leads to improve the agreement with the experimental measurements in the near wall region. Numerical results from the DEM-CFD approach were also compared with TFM numerical predictions available from the literature (Fede et al. (2016)). The latter were obtained by an Euler-Euler modeling using closures formulated in the frame of a statistical PDF approach (Balzer et al. (1995), Boelle et al. (1995)). Comparisons were carried out with the same collision parameters in order to evaluate the overall Eulerian modeling, including the boundary conditions formulated in the frame of the KTGF approach. Globally, DEM-CFD and TFM results were found in very good agreement for frictionless conditions. Both the approaches exhibited high

sensitivity to the normal particle-particle restitution coefficient, which substantially modifies the particulate flow behavior due to the effect of the energy dissipation by inelastic collisions on the bubble rate formation. DEM-CFD results were also compared with TFM numerical predictions obtained using smooth wall boundary conditions with friction (Fede et al. (2016)), in the frame of Coulomb's frictional sliding. In the pressurized fluidized bed, the effective friction effect predicted by the DEM-CFD simulations at the wall was found quite larger compared to that observed from TFM results. In order to understand such a difference and to characterize the particle-wall interactions at mesoscopic scale, a detailed local analysis in the near wall region was carried out. Such an analysis was realized in the frame of the soft-sphere DEM-CFD with the intent to provide information about the boundary conditions for a TFM simulations. By estimating the force per unit area applied by the particles on the wall, it has been shown that the particle-wall mean momentum transfer is due to both the effect of the short time collisions, typical of dilute regime, and to the long sustained particle contacts with wall due to sliding of clusters in the near wall region. So, according to the DEM-CFD simulation results, the particle-wall frictional stress contribution has to be accounted for in the particle resolved velocity wall boundary conditions to improve the predictions of dense fluidized beds using the TFM approach.

Aknowledgement

This work received funding from Agence national de la recherche (ANR) through the project MORE4LESS. It was granted access to the HPC resources of CINES supercomputing center under the allocations A0012B07345 and A0062B10864. CINES is gratefully acknowledged. The authors wish to thank Dr. Pascal Fede for providing data from experiments and from TFM numerical simulations, and Dr. Ghislain Lartigue for his support with YALES2.

References

Amritkar, A., Deb, S., Tafti, D., 2014. Efficient parallel CFD-DEM simulations using OpenMP. Journal of Computational Physics 256, 501–519.

Balachandar, S., Eaton, J. K., 2010. Turbulent dispersed multiphase flow. Annual Review of Fluid Mechanics 42 (1), 111–133.

Balzer, G., Boelle, A., Simonin, O., 1995. Eulerian gas-solid flow modelling of dense fluidized bed. In: FLUIDIZATION VIII, International Symposium of the Engineering Foundation. J.F. Large and C. Laguérie (Editors), published in 1996 by Engineering Foundation, pp. 409–418.

Berger, R., Kloss, C., Kohlmeyer, A., Pirker, S., 2015. Hybrid parallelization of the LIGGGHTS open-source DEM code. Powder Technology 278, 234–247.

Bernard, M., Climent, E., Wachs, A., 2016. Controlling the quality of two-way Euler/Lagrange numerical modeling of bubbling and spouted fluidized beds dynamics. Industrial & Engineering Chemistry Research 56 (1), 368–386.

Boelle, A., Balzer, G., Simonin, O., 1995. Second-order prediction of the particle-phase stress tensor of inelastic spheres in simple shear dense suspensions. In: Gas-Particle Flows, ASME FED. Vol. 228. pp. 9–18.

Buist, K. A., Seelen, L., Deen, N., Padding, J., Kuipers, J., 2016. On an efficient hybrid soft and hard sphere collision integration scheme for dem. Chemical Engineering Science 153, 363–373.

Capecelatro, J., Desjardins, O., 2013. An Euler–Lagrange strategy for simulating particle-laden flows. Journal of Computational Physics 238, 1–31.

Cundall, P., Strack, O., 1979. A discrete numerical model for granular assemblies. Geotechnique 29 (1), 47–65.

Dan, S., Shuyan, W., Huilin, L., Zhiheng, S., Xiang, L., Shuai, W., Yunhua, Z., Lixin, W., 2009. A second-order moment method of dense gas–solid flow for bubbling fluidization. Chemical Engineering Science 64 (23).

Deen, N. G., Annaland, M. V. S., Van der Hoef, M. A., Kuipers, J. A. M., 2007. Review of discrete particle modeling of fluidized beds. Chemical Engineering Science 62 (1-2), 28–44.

Deen, N. G., Peters, E. A. J. F., Padding, J. T., Kuipers, J. A. M., 2014. Review of direct numerical simulation of fluid–particle mass, momentum and heat transfer in dense gas–solid flows. Chemical Engineering Science 116, 710 – 724.

Dufresne, Y., Lartigue, G., Moureau, V., Masi, E., Simonin, O., 2019. High Performance CFD/DEM Approach in Complex Geometries on Unstructured Meshes. In: Direct and Large-Eddy Simulation XI. Springer, pp. 193–199.

Dufresne, Y., Moureau, V., Lartigue, G., Simonin, O., 2020. A massively parallel CFD/DEM approach for reactive gas-solid flows in complex geometries using unstructured meshes. Computers & Fluids 198, 104402.

Dufresne, Y., Moureau, V., Masi, E., Simonin, O., Horwitz, J., 2016. Simulation of a reactive fluidized bed reactor using CFD/DEM. In: Proceeding of Center for Turbulence Research Summer Program 2016. pp. 35–44.

Ergun, S., 1952. Fluid flow through packed columns. Chem. Eng. Prog. 48, 89–94.

Fede, P., Moula, G., Ingram, A., Dumas, T., Simonin, O., 2009. 3D Numerical simulation and PEPT experimental investigation of pressurized gas-solid fluidized bed hydrodynamic. In: Proc. 12th Int. Symp. on Gas-Particle Flows, 2009 ASME Fluids Engineering Summer Conference, Vail (USA), FEDSM2009-78048.

Fede, P., Simonin, O., 2006. Numerical study of the subgrid fluid turbulence effects on the statistics of heavy colliding particles. Physics of Fluids 18 (4), 045103.

Fede, P., Simonin, O., Ingram, A., 2016. 3D numerical simulation of a lab-scale pressurized dense fluidized bed focussing on the effect of the particle-particle restitution coefficient and particle–wall boundary conditions. Chemical Engineering Science 142, 215–235.

Feng, Y.-Q., Pinson, D., Yu, A.-B., Chew, S. J., Zulli, P., 2003. Numerical study of gas-solid flow in the raceway of a blast furnace. Steel Research International 74 (9), 523–530.

Février, P., Simonin, O., Squires, K. D., 2005. Partitioning of particle velocities in gas–solid turbulent flows into a continuous field and a spatially uncorrelated random distribution: theoretical formalism and numerical study. Journal of Fluid Mechanics 533.

Foerster, S. F., Louge, M. Y., Chang, H., Allia, K., 1994. Measurements of the collision properties of small spheres. Physics of Fluids 6 (3), 1108–1115.

Fox, R. O., 2014. On multiphase turbulence models for collisional fluid-particle flows. Journal of Fluid Mechanics 742, 368.

Gatignol, R., 1983. The Faxén formulas for a rigid particle in an unsteady non-uniform Stokes-flow. Journal de Mécanique Théorique et Appliquée 2 (2), 143–160.

Gidaspow, D., 1994. Multiphase flow and fluidization: continuum and kinetic theory descriptions. Academic press.

Gobin, A., Neau, H., Simonin, O., Llinas, J.-R., Reiling, V., Sélo, J.-L., 2003. Fluid dynamic numerical simulation of a gas phase polymerization reactor. International Journal for Numerical Methods in Fluids 43 (10-11), 1199–1220.

Goldschmidt, M., Beetstra, R., Kuipers, J., 2002. Hydrodynamic modelling of dense gas-fluidised beds: Comparison of the kinetic theory of granular flow with 3D hard-sphere discrete particle simulations. Chemical Engineering Science 57 (11), 2059 – 2075.

Goldschmidt, M., Kuipers, J., van Swaaij, W. P. M., 2001. Hydrodynamic modelling of dense gas-fluidised beds using the kinetic theory of granular flow: effect of coefficient of restitution on bed dynamics. Chemical Engineering Science 56 (2).

Goniva, C., Kloss, C., Deen, N. G., Kuipers, J. A., Pirker, S., 2012. Influence of rolling friction on single spout fluidized bed simulation. Particuology 10 (5), 582–591.

Guo, Y., Curtis, J. S., 2015. Discrete element method simulations for complex granular flows. Annual Review of Fluid Mechanics 47, 21–46.

Hamidouche, Z., Dufresne, Y., Pierson, J.-L., Brahem, R., Lartigue, G., Moureau, V., 2019. DEM/CFD Simulations of a Pseudo-2D Fluidized Bed: Comparison with Experiments. Fluids 4 (1), 51.

Hamidouche, Z., Masi, E., Fede, P., Ansart, R., Neau, H., Hemati, M., Simonin, O., 2018. Chapter two - numerical simulation of multiphase reactive flows. In: Parente, A., De Wilde, J. (Eds.), Bridging Scales in Modelling and Simulation of Non-Reacting and Reacting Flows. Part I. Vol. 52 of Advances in Chemical Engineering. Academic Press, pp. 51 – 124.

Hoomans, B., Kuipers, J., Briels, W. J., van Swaaij, W. P. M., 1996. Discrete particle simulation of bubble and slug formation in a two-dimensional gas-fluidised bed: a hard-sphere approach. Chemical Engineering Science 51 (1), 99–118.

Hui, K., Haff, P., Ungar, J., Jackson, R., 1984. Boundary conditions for high-shear grain flows. Journal of Fluid Mechanics 145, 223–233.

Ijzermans, R. H. A., Meneguz, E., Reeks, M. W., 2010. Segregation of particles in incompressible random flows: singularities, intermittency and random uncorrelated motion. Journal of Fluid Mechanics 653, 99–136.

Jajcevic, D., Siegmann, E., Radeke, C., Khinast, J. G., 2013. Large-scale CFD–DEM simulations of fluidized granular systems. Chemical Engineering Science 98, 298–310.

Jenkins, J., 1992. Boundary conditions for rapid granular flow: flat, frictional walls. Journal of Applied Mechanics 59 (1), 120–127.

Jenkins, J. T., Savage, S. B., 1983. A theory for the rapid flow of identical, smooth, nearly elastic, spherical particles. Journal of Fluid Mechanics 130, 187–202.

Johnson, P. C., Jackson, R., 1987. Frictional–collisional constitutive relations for granular materials, with application to plane shearing. Journal of Fluid Mechanics 176, 67–93.

Johnson, P. C., Nott, P., Jackson, R., 1990. Frictional-collisional equations of motion for participate flows and their application to chutes. Journal of Fluid Mechanics 210, 501–535.

Jung, J., Gidaspow, D., Gamwo, I. K., 2005. Measurement of two kinds of granular temperatures, stresses, and dispersion in bubbling beds. Industrial & Engineering Chemistry Research 44 (5), 1329–1341.

Kaneko, Y., Shiojima, T., Horio, M., 1999. DEM simulation of fluidized beds for gas-phase olefin polymerization. Chemical Engineering Science 54 (24), 5809–5821.

Kaufmann, A., Moreau, M., Simonin, O., Helie, J., 2008. Comparison between Lagrangian and mesoscopic Eulerian modelling approaches for inertial particles suspended in decaying isotropic turbulence. Journal of Computational Physics 227 (13), 6448–6472.

Kawaguchi, T., Tanaka, T., Tsuji, Y., 1998. Numerical simulation of two-dimensional fluidized beds using the discrete element method (comparison between the two-and three-dimensional models). Powder Technology 96 (2), 129–138.

Kloss, C., Goniva, C., Hager, A., Amberger, S., Pirker, S., 2012. Models, algorithms and validation for opensource DEM and CFD-DEM. Progress in Computational Fluid Dynamics, An International Journal 12 (2-3), 140–152.

Konan, N., Kannengieser, O., Simonin, O., 2009. Stochastic modeling of the multiple rebound effects for particle–rough wall collisions. International Journal of Multiphase Flow 35 (10), 933–945.

Kuerten, J. G. M., 2016. Point-Particle DNS and LES of Particle-Laden Turbulent flow - a state-of-the-art review. Flow, Turbulence and Combustion 97 (3), 689–713.

Li, J., Kuipers, J. A. M., 2007. Effect of competition between particle–particle and gas–particle interactions on flow patterns in dense gas-fluidized beds. Chemical Engineering Science 62 (13), 3429–3442.

Li, T., Garg, R., Galvin, J., Pannala, S., 2012. Open-source MFIX-DEM software for gas-solids flows: Part II - Validation studies. Powder Technology 220, 138–150.

Li, Z., Janssen, T., Buist, K., Deen, N., van Sint Annaland, M., Kuipers, J., 2017. Experimental and simulation study of heat transfer in fluidized beds with heat production. Chemical Engineering Journal 317, 242 – 257.

Link, J., Cuypers, L., Deen, N., Kuipers, J., 2005. Flow regimes in a spout–fluid bed: A combined experimental and simulation study. Chemical Engineering Science 60 (13), 3425 – 3442.

Masi, E., Simonin, O., Riber, E., Sierra, P., Gicquel, L. Y., 2014. Development of an algebraic-closure-based moment method for unsteady Eulerian simulations of particle-laden turbulent flows in very dilute regime. International Journal of Multiphase Flow 58, 257–278.

Maxey, M. R., Riley, J. J., 1983. Equation of motion for a small rigid sphere in a nonuniform flow. Physics of Fluids 26 (4), 883–889.

Mikami, T., Kamiya, H., Horio, M., 1998. Numerical simulation of cohesive powder behavior in a fluidized bed. Chemical Engineering Science 53 (10), 1927–1940.

Moreau, M., Simonin, O., Bédat, B., 2010. Development of gas-particle Euler-Euler LES approach: A priori analysis of particle sub-grid models in homogeneous isotropic turbulence. Flow, Turbulence and Combustion 84, 295–324.

Moureau, V., Domingo, P., Vervisch, L., 2011. Design of a massively parallel cfd code for complex geometries. Comptes Rendus Mécanique 339 (2-3), 141–148.

Müller, C. R., Holland, D. J., Sederman, A. J., Scott, S. A., Dennis, J. S., Gladden, L. F., 2008. Granular temperature: comparison of magnetic resonance measurements with discrete element model simulations. Powder Technology 184 (2), 241–253.

Neuwirth, J., Antonyuk, S., Heinrich, S., Jacob, M., 2013. CFD–DEM study and direct measurement of the granular flow in a rotor granulator. Chemical Engineering Science 86, 151 – 163.

Nigmetova, A., Dufresne, Y., Masi, E., Moureau, V., Simonin, O., 2021. Soft-sphere DEM simulation of coarse particles transported by a fully developed turbulent gas vertical channel flow. In: Turbulence and Interactions - Proceedings of the TI 2018 Conference, June 25-29, 2018, Les Trois-Îlets, Martinique, France.

Ocone, R., Sundaresan, S., Jackson, R., 1993. Gas-particle flow in a duct of arbitrary inclination with particle-particle interactions. AIChE Journal 39 (8), 1261–1271.

Parker, D. J., Leadbeater, T. W., Fan, X., Hausard, M. N., Ingram, A., Yang, Z., 2008. Positron imaging techniques for process engineering: recent developments at Birmingham. Measurement Science and Technology 19 (9), 094004.

Patil, A., Peters, E., Kuipers, J., 2015. Comparison of CFD–DEM heat transfer simulations with infrared/visual measurements. Chemical Engineering Journal 277, 388–401.

Patil, D. J., van Sint Annaland, M., Kuipers, J. A. M., 2005a. Critical comparison of hydrodynamic models for gas-solid fluidized beds - part I : bubbling gas-solid fluidized beds operated with a jet. Chemical Engineering Science 60 (1), 57–72.

Patil, D. J., van Sint Annaland, M., Kuipers, J. A. M., 2005b. Critical comparison of hydrodynamic models for gas-solid fluidized beds - part II: freely bubbling gas-solid fluidized beds. Chemical Engineering Science 60 (1), 73–84.

Pepiot, P., Desjardins, O., 2012. Numerical analysis of the dynamics of two-and three-dimensional fluidized bed reactors using an Euler–Lagrange approach. Powder Technology 220, 104–121.

Radenkovic, D., Simonin, O., 2018. Stochastic modelling of three-dimensional particle rebound from isotropic rough wall surface. International Journal of Multiphase Flow 109, 35–50.

Sakiz, M., Simonin, O., 1999. Development and validation of continuum particle wall boundary conditions using lagrangian simulation of a vertical gas-solid channel flow. In: Proc. 8th Int. Symp. on Gas-Particle Flows, ASME Fluids Engineering Division Summer Meeting, FEDSM99-7898.

Schneiderbauer, S., Aigner, A., Pirker, S., 2012. A comprehensive frictional-kinetic model for gas–particle flows: Analysis of fluidized and moving bed regimes. Chemical Engineering Science 80, 279–292.

Schwarzkopf, J. D., Sommerfeld, M., Crowe, C. T., Tsuji, Y., 2011. Multiphase flows with droplets and particles. CRC press.

Seville, J. P. K., Ingram, A., Parker, D. J., 2005. Probing processes using positrons. Chemical Engineering Research and Design 83 (7), 788 – 793.

Simonin, O., Février, P., Laviéville, J., 2002. On the spatial distribution of heavy-particle velocities in turbulent flow: from continuous field to particulate chaos. Journal of Turbulence 3, N40.

Soleimani, A., Pirker, S., Schneiderbauer, S., 2015. Solid boundary condition for collisional gas-solid flows at rough walls. Powder Technology 281, 28–33.

Sommerfeld, M., Huber, N., 1999. Experimental analysis and modelling of particle-wall collisions. International Journal of Multiphase Flow 25 (6), 1457–1489.

Sutkar, V. S., Deen, N. G., Patil, A. V., Salikov, V., Antonyuk, S., Heinrich, S., Kuipers, J. A., 2016. CFD-DEM model for coupled heat and mass transfer in a spout fluidized bed with liquid injection. Chemical Engineering Journal 288, 185–197.

Tenneti, S., Subramaniam, S., 2014. Particle-resolved direct numerical simulation for gas-solid flow model development. Annual Review of Fluid Mechanics 46 (1), 199–230.

Tsuji, Y., Kawaguchi, T., Tanaka, T., 1993. Discrete particle simulation of two-dimensional fluidized bed. Powder Technology 77 (1), 79–87.

Tsuji, Y., Tanaka, T., Ishida, T., 1992. Lagrangian numerical simulation of plug flow of cohesionless particles in a horizontal pipe. Powder Technology 71 (3), 239–250.

van Buijtenen, M. S., van Dijk, W.-J., Deen, N. G., Kuipers, J., Leadbeater, T., Parker, D., 2011. Numerical and experimental study on multiple-spout fluidized beds. Chemical Engineering Science 66 (11), 2368 – 2376.

van der Hoef, M. A., Ye, M., van Sint Annaland, M., Andrews, A. T., Sundaresan, S., Kuipers, J. A. M., 2006. Multiscale modeling of gas-fluidized beds. In: Marin, G. B. (Ed.), Computational Fluid Dynamics. Vol. 31 of Advances in Chemical Engineering. Academic Press, pp. 65 – 149.

Vance, M. W., Squires, K. D., Simonin, O., 2006. Properties of the particle velocity field in gas-solid turbulent channel flow. Physics of Fluids 18 (6), 063302.

Vié, A., Doisneau, F., Massot, M., 2015. On the anisotropic gaussian velocity closure for inertial-particle laden flows. Communications in Computational Physics 17 (1), 1–46.

Wen, C. Y., Yu, Y. H., 1966. Mechanics of fluidization. Chemical Engineering Symposium Series 62, 100–111.

Xu, B., Yu, A., 1997. Numerical simulation of the gas-solid flow in a fluidized bed by combining discrete particle method with computational fluid dynamics. Chemical Engineering Science 52 (16), 2785–2809.

Yang, L., Padding, J. T., Kuipers, J. A. M., 2017. Investigation of collisional parameters for rough spheres in fluidized beds. Powder Technology 316, 256–264.

Yuu, S., Umekage, T., Johno, Y., 2000. Numerical simulation of air and particle motions in bubbling fluidized bed of small particles. Powder Technology 110 (1-2), 158–168.

Zhu, H. P., Zhou, Z. Y., Yang, R. Y., Yu, A. B., 2007. Discrete particle simulation of particulate systems: Theoretical developments. Chemical Engineering Science 62 (13), 3378 – 3396.

Zhu, H. P., Zhou, Z. Y., Yang, R. Y., Yu, A. B., 2008. Discrete particle simulation of particulate systems: a review of major applications and findings. Chemical Engineering Science 63 (23), 5728–5770.